Numerical study of the steady-state uniform flow past a rotating cylinder

By J. C. PADRINO and D. D. JOSEPH†

Department of Aerospace Engineering and Mechanics, University of Minnesota,
Minneapolis, MN 55455, USA

Results from the numerical simulation of the two-dimensional incompressible unsteady Navier–Stokes equations for streaming flow past a rotating circular cylinder are presented in this study. The numerical solution of the equations of motion is conducted with a commercial computational fluid dynamics package which discretizes the equations applying the control volume method. The numerical set-up is validated by comparing results for a Reynolds number based on the free stream of $Re = 200$ and dimensionless peripheral speed of $\tilde{q} = 3$, 4 and 5 with results from the literature. After the validation stage, various pairs of Re and $\tilde{q}$ are specified in order to carry out the numerical experiments. These values are $Re = 200$ with $\tilde{q} = 4$ and 5; $Re = 400$ with $\tilde{q} = 4$, 5 and 6, and $Re = 1000$ with $\tilde{q} = 3$. In all these cases, gentle convergence to fully developed steady state is reached. From the numerical vorticity distribution, the position of the outer edge of the vortical region is determined as a function of the angular coordinate. This position is found by means of a reasonable criterion set to define the outmost curve around the cylinder where the vorticity magnitude reaches a certain cut-off value. By considering the average value of this profile, a uniform vortical region thickness is specified for every pair of Re and $\tilde{q}$.

Next, the theoretical approach of Wang & Joseph (2006a; see the companion paper) and the numerical results are used to determine two different values of the effective vortical region thickness for every pair of Re and $\tilde{q}$. One effective thickness δ_D/a is obtained from the match between the additional drag on the outer edge of the vortical region according to the viscous correction of viscous potential flow (VCVPF) and the corresponding numerical profile while the other thickness δ_L/a is determined from the match between the pressure lift on the cylinder obtained from Wang & Joseph (2006a)'s simple modification of the boundary-layer analysis due to Glauert (*Proc. R. Soc. Lond.* A, vol. 242, 1957, p. 108) and the numerical value of the pressure lift coefficient. The values of δ_D/a and δ_L/a are used in the computation of various parameters associated with the flow, namely, the torque on the rotating cylinder, the circulatory velocity at the edge of the vortical region, which links the cylinder's angular velocity with the circulation of the irrotational flow of the viscous fluid outside this region, and the viscous dissipation. Predictions from the approaches of Glauert (1957) and Wang & Joseph (2006a) are also included for comparison. The values of both effective thicknesses, δ_D/a and δ_L/a, are found to have the same order of magnitude. Then, we show that choosing δ_D/a as a unique effective thickness, the modification of Glauert's boundary-layer analysis and the VCVPF approach as proposed by Wang &

† Author to whom correspondence should be addressed: joseph@aem.umn.edu

Joseph (2006*a*) produce results which are in better general agreement with the values from numerical simulation than those from Glauert's solution.

___

1. Introduction

A rapidly rotating circular cylinder immersed in a free stream generates a fluid motion that has been the subject of research from the point of view of numerical simulations, experiments and theoretical analysis. This flow field is equivalent to the one obtained when a circular cylinder rotates and translates through a fluid at rest at infinity as seen from a reference frame that translates with the centre of the cylinder. This type of fluid motion is of major importance in aerodynamics, since fundamental aspects of the flow past an airfoil can be enlightened through conformal transformation from the flow past a rotating cylinder, under the appropriate simplifications. It has also been the topic of research for boundary-layer control and drag reduction over the years (Ece, Walker & Doligalski 1984; He *et al.* 2000).

Two aspects have drawn attention from researchers with respect to streaming flow past a rotating circular cylinder. The first aspect is the observation that the spinning action is able to suppress the separation of the boundary layer around the cylinder as well as to avoid vortex shedding from the surface of the cylinder while reaching steady state when a critical dimensionless velocity is achieved. This threshold has been reported to be a function of the Reynolds number of the free stream. The second aspect is the lift generated on the cylinder by the surrounding fluid, also known as the Magnus effect. Prandtl's famous limiting value of the lift force generated by a rotating circular cylinder has encountered contradictory evidence from theoretical studies, experiments and computations (e.g., Glauert 1957; Tokumaru & Dimotakis 1993; Mittal & Kumar 2003), thus making this problem even more attractive as the subject for improved numerical methods and experimental techniques.

The literature reveals that two relevant parameters are usually specified to describe the problem, namely, the Reynolds number $Re = 2U_0 a/\nu$, based on the free-stream velocity U_0, the diameter of the cylinder $2a$ and fluid kinematic viscosity ν, and the dimensionless peripheral velocity $\tilde{q}$, defined as the ratio of the velocity magnitude at the surface of the cylinder to the free-stream velocity. From the point of view of the numerical simulations, setting the appropriate range for these parameters is a delicate task on which part of the success of the numerical work relies. Another feature is the choice of the form of the governing equations to solve. For a two-dimensional problem, the vorticity and streamfunction form of the Navier–Stokes equations is the preferred option. However, some numerical work has been carried out with the equations of motion written in terms of the primitive variables, velocity and pressure. Ingham (1983) obtained numerical solutions of the two-dimensional steady incompressible Navier–Stokes equations in terms of vorticity and streamfunction using finite differences for flow past a rotating circular cylinder for Reynolds numbers $Re = 5$ and 20 and dimensionless peripheral velocity $\tilde{q}$ between 0 and 0.5. Solving the same form of the governing equations, but expanding the range for $\tilde{q}$, Ingham & Tang (1990) showed numerical results for $Re = 5$ and 20 and $0 \leqslant \tilde{q} \leqslant 3$. With a substantial increase in Re, Badr *et al.* (1990) studied the unsteady two-dimensional flow past a circular cylinder which translates and rotates starting impulsively from rest both numerically and experimentally for $10^3 \leqslant Re \leqslant 10^4$ and $0.5 \leqslant \tilde{q} \leqslant 3$. They solved the unsteady equations of motion in terms of vorticity and streamfunction. The agreement

between numerical and experimental results was good except for the highest rotational velocity where they observed three-dimensional and turbulence effects. Choosing a moderate interval for Re, Tang & Ingham (1991) followed with numerical solutions of the steady two-dimensional incompressible equations of motion for $Re = 60$ and 100 and $0 \leqslant \tilde{q} \leqslant 1$. They employed a scheme that avoids the difficulties regarding the boundary conditions far from the cylinder.

Considering a moderate constant $Re = 100$, Chew, Cheng & Luo (1995) further expanded the interval for the dimensionless peripheral velocity $\tilde{q}$, such that $0 \leqslant \tilde{q} \leqslant 6$. They used a vorticity streamfunction formulation of the incompressible Navier–Stokes equations. The numerical method consisted of a hybrid vortex scheme, where the time integration is split into two fractional steps, namely, pure diffusion and convection. They separated the domain into two regions: the region close to the cylinder where viscous effects are important and the outer region where viscous effects are neglected and potential flow is assumed. Using the expression for the boundary-layer thickness for flow past a flat plate, they estimated the thickness of the inner region. Their results indicated a critical value for $\tilde{q}$ about 2 where vortex shedding ceases and the lift and the drag coefficients tend to asymptotic values. Nair, Sengupta & Chauhan (1998) expanded their choices for the Reynolds number by selecting a moderate $Re = 200$ with $\tilde{q} = 0.5$ and 1 and two relatively high values of $Re = 1000$ and $Re = 3800$, with $\tilde{q} = 3$ and $\tilde{q} = 2$, respectively. They performed the numerical study of flow past a translating and rotating circular cylinder solving the two-dimensional unsteady Navier–Stokes equations in terms of vorticity and streamfunction using a third-order upwind scheme. Kang, Choi & Lee (1999) followed with the numerical solution of the unsteady governing equations in the primitive variables velocity and pressure for flows with $Re = 60$, 100 and 160 with $0 \leqslant \tilde{q} \leqslant 2.5$. Their results showed that vortex shedding vanishes when $\tilde{q}$ increases beyond a critical value which follows a logarithmic dependence on the Reynolds number (e.g., the critical dimensionless peripheral velocity $\tilde{q} = 1.9$ for $Re = 160$).

Chou (2000) worked in the area of high Reynolds numbers by presenting a numerical study that included computations falling into two categories: $\tilde{q} \leqslant 3$ with $Re = 10^3$ and $\tilde{q} \leqslant 2$ with $Re = 10^4$. Chou solved the unsteady two-dimensional incompressible Navier–Stokes equations written in terms of vorticity and streamfunction. In contrast, the work of Mittal & Kumar (2003) performed a comprehensive numerical investigation by fixing a moderate value of $Re = 200$ while considering a wide interval for the dimensionless peripheral velocity of $0 \leqslant \tilde{q} \leqslant 5$. They used the finite-element method to solve the unsteady incompressible Navier–Stokes equations in two-dimensions for the primitive variables velocity and pressure. They observed vortex shedding for $\tilde{q} < 1.91$. Steady-state fully developed flow was achieved for higher rotation rates except for the narrow region $4.34 < \tilde{q} < 4.8$ where vortex shedding was again reported, perhaps, for the first time. This literature survey indicates that workers have favoured moderate Reynolds numbers $Re \leqslant 200$ in order to keep the turbulence effects away and to prevent the appearance of non-physical features in their numerical results. For similar reasons, the peripheral speeds have been chosen such that $\tilde{q} \leqslant 3$ in most of the cases, whereas few workers have simulated beyond this value, with $\tilde{q} = 6$ as an upper bound.

In comparison with the substantial number of studies devoted to the numerical investigation of streaming flow past a rotating circular cylinder, fewer studies have focused on the theoretical approach of this problem. Boundary-layer analysis, which considers irrotational flow outside, has been the preferred strategy to theoretically approximate the solution for this type of fluid motion. The celebrated work of Glauert

(1957) developed an approximate solution of the boundary-layer equations as a power series in terms of the ratio of the free-stream velocity to the peripheral velocity of the cylinder's surface. Outside the boundary layer, Glauert assumed irrotational steady-state flow past a circular cylinder with circulation, whereas the thickness of the boundary layer is considered very thin, and thus neglected to the order of his approximation. Furthermore, he presented expressions for the lift and torque on the cylinder. He did not account for the effects of friction in the lift. According to Glauert's results, the lift force on the cylinder increases indefinitely as the peripheral velocity increases, which contradicts Prandtl's classical limiting value. Moore (1957) presented a solution for the flow past a rotating circular cylinder by considering the effect of the uniform free stream as a small perturbation on the solution for purely rotary flow created by the spinning cylinder. Moore's solution gives rise to a zero drag force on the cylinder while the lift force is expressed by the classical formula as a function of the circulation. Ece *et al.* (1984) studied the boundary-layer development for the flow past a circular cylinder impulsively started into translation and rotation. They focused on the unsteady stage of the motion to address the effect of the rotational speed on separation. They considered an expansion of the solution in a power series in time and performed their calculations for various peripheral speeds of the cylinder's wall and the limit of *Re* going to infinity. They compared their results with values computed from the numerical solutions of the governing equations and excellent agreement was reported throughout the early phases of the motion.

In a companion paper, Wang & Joseph (2006*a*; hereinafter called WJa) applied their viscous correction of viscous potential flow theory (VCVPF) to analyse the boundary-layer problem for the flow past a rapidly rotating solid circular cylinder where the separation is suppressed. They modified the boundary-layer analysis proposed by Glauert (1957) to take into account the viscous irrotational rotary flow in the boundary-layer solution. In their analysis, the boundary-layer thickness, which is not completely neglected, must be prescribed. Using the results from their modified boundary-layer analysis, WJa showed that there is a discrepancy at the outer edge of the boundary layer between the shear stress given by their analysis and the shear stress calculated from the irrotational flow theory. A viscous pressure correction is then induced by this discrepancy. By equating the power of the pressure correction to the power of the shear stress discrepancy, WJa determined an expression for the drag force acting on the cylinder as a function of the boundary-layer thickness. The VCVPF theory has been successfully applied to different problems in fluid mechanics such as the drag on a spherical gas bubble, the drag on a liquid drop rising in another liquid (Joseph & Wang 2004) and the capillary instability (Wang, Joseph & Funada 2005). In a second companion paper Wang & Joseph (2006*b*; hereinafter called WJb) presented a new boundary-layer analysis for streaming flow past a rapidly rotating circular cylinder. They assumed that a boundary layer is attached to the surface of the rotating cylinder, while, outside the boundary layer, irrotational flow of a viscous fluid is considered. In the interior of the boundary layer, the velocity field is separated into a boundary-layer-flow component and an irrotational purely rotary-flow component. Beyond the outer edge of the boundary layer, the flow is decomposed into an irrotational flow past a fixed cylinder and an irrotational purely rotary flow. Then, they inserted the velocity decomposition inside the boundary layer into the governing equations without any approximation. They solved the resulting new set of equations using Glauert's series method, enforcing continuity of the shear stress at the outer edge of the boundary layer. In their analysis, the pressure inside the boundary layer cannot be assumed constant in the direction normal to the wall.

Many studies have been devoted to the numerical simulation of this type of fluid motion to address the problem of presence or suppression of separation and vortex shedding. However, rather less attention has been paid to the application of numerical results to delimit and describe the region around the cylinder where vorticity effects are far from negligible. This fluid zone is named the vortical region. Once this region is delimited, the evaluation of theoretical boundary-layer-type solutions is feasible. When Re and $\tilde{q}$ are not so high, say $Re < 1000$ and $\tilde{q} < 5$, the vortical region can be relatively thick, so the classical thin boundary-layer analysis may not work with acceptable accuracy; nevertheless, there is still an identifiable region where the effects of vorticity are significant. Outside this region, the potential flow theory for flow past a circular cylinder with circulation may be applied.

This study pursues two main objectives. The first objective is to simulate numerically the steady-state limit of the flow past a rotating circular cylinder. The second objective is to bound the region around the rotating cylinder where the vorticity effects are mostly confined. The numerical results presented in this paper are intended to test the validity of the theoretical approaches of WJa and WJb. A value for an effective, uniform thickness of the vortical region must be prescribed in these models. The flow field obtained from numerical analysis represents reliable data that can be used to estimate the limits of the vortical region. The numerical simulations are performed by solving the two-dimensional incompressible unsteady Navier–Stokes equations using the commercial package Fluent® 6.1 (2003). Tests of mesh refinement were used to select the size of the computational domain and mesh structure. Validation of the numerical set-up is performed comparing our results with those from the literature for three cases.

Next, the velocity and pressure fields are computed for Reynolds numbers based on the free-stream velocity $Re = 200$ and 400, with dimensionless peripheral velocity $\tilde{q} = 4$, 5 and 6. Results for $Re = 1000$ with $\tilde{q} = 3$ are also considered. The drag and lift coefficients on the rotating cylinder are presented. From the numerical vorticity distribution in the fluid domain, the position of the outer edge of the vortical region is determined as a function of the angular coordinate. This position is found by means of a reasonable criterion set to define the outmost curve around the cylinder where the vorticity magnitude reaches a certain cutoff value. By considering the average value of this profile, a uniform vortical region thickness is specified for every pair of Re and $\tilde{q}$. The selection of this cutoff value is somewhat arbitrary, and moderate changes in this parameter may yield significant changes in the extension of the vortical region. This feature motivates the introduction of an effective vortical region thickness, which represents an alternative approach to define the position of the outer edge of the vortical region. The theoretical approach of WJa and the numerical results are used to determine two different values of the effective vortical region thickness for every pair of Re and $\tilde{q}$. One effective thickness is obtained from the match between the additional drag on the outer edge of the vortical region according to VCVPF and the corresponding numerical profile, while the other thickness is determined from the match between the pressure lift on the cylinder obtained from WJa's simple modification of Glauert's boundary-layer analysis and the numerical value of the pressure lift coefficient. The first effective vortical region thickness is employed in the computation of the circulatory velocity at the edge of the vortical region and the viscous dissipation inside and outside this region from the numerical velocity field. These numerical results are compared with predictions from expressions by WJa computed using this effective vortical region thickness. The second effective vortical region thickness is used in the approach of WJa to predict the torque coefficient

on the rotating body. This result is compared with the corresponding value from the numerical simulations. In addition, predictions from the classical boundary-layer analysis of Glauert (1957) are included and discussed along with the previous results. Glauert's approach does not require the thickness of the boundary layer to be specified. Exhaustive comparisons are also presented and discussed in WJa and WJb.

2. Numerical features

The two-dimensional unsteady incompressible Navier–Stokes equations are the governing expressions for the problem at hand. In dimensionless form, these equations can be written as:

$$\frac{\partial \tilde{\boldsymbol{u}}}{\partial \tilde{t}} + \tilde{\boldsymbol{u}} \cdot \nabla \tilde{\boldsymbol{u}} = -\nabla \tilde{p} + \frac{1}{Re} \nabla^2 \tilde{\boldsymbol{u}}, \tag{2.1}$$

and

$$\nabla \cdot \tilde{\boldsymbol{u}} = 0, \tag{2.2}$$

on a domain Φ with boundaries Λ and subject to appropriate boundary conditions. The tilde designates dimensionless variables. Unless otherwise noted, the following scales are considered to make the equations dimensionless:

$$[\text{length, velocity, time, pressure}] \equiv \left[2a, \ U_0, \ \frac{2a}{U_0}, \ \rho U_0^2 \right]. \tag{2.3}$$

Three relevant parameters computed from the velocity and pressure fields are the drag, lift and torque coefficients, which represent dimensionless expressions of the forces and torque that the fluid produces on the circular cylinder. These are defined, respectively, as follows:

$$C_D = \frac{D}{\rho U_0^2 a}, \qquad C_L = \frac{L}{\rho U_0^2 a}, \qquad C_T = \frac{T}{2\rho U_0^2 a^2}, \tag{2.4}$$

where D is the drag force, L is the lift force and T is the torque with respect to the centre of the cylinder.

The numerical solution of the governing system of partial differential equations is carried out through the computational fluid dynamics package Fluent® 6.1. This computer program applies a control-volume method to integrate the equations of motion, constructing a set of discrete algebraic equations with conservative properties. The segregated numerical scheme, which solves the discretized governing equations sequentially, is selected. An implicit scheme is applied to obtain the discretized system of equations. The sequence updates the velocity field through the solution of the momentum equations using known values for pressure and velocity. Then, it solves a 'Poisson-type' pressure correction equation obtained by combining the continuity and momentum equations. A quadratic upwind interpolation for convective kinematics (QUICK) scheme is used to discretize the convective term in the momentum equations. Pressure-implicit with splitting of operators (PISO) is selected as the pressure-velocity coupling scheme. Finally, the time integration of the unsteady momentum equations is performed using a second-order approximation.

Although, from a mathematical point of view, the problem set-up imposes boundary conditions at infinity, the numerical approach necessarily considers a finite computational domain. Hence, there is an outer boundary where inflow and outflow boundary conditions should be applied. Figure 1 shows the computational domain and the reference frames selected for this study. We use a modified O-type mesh similar
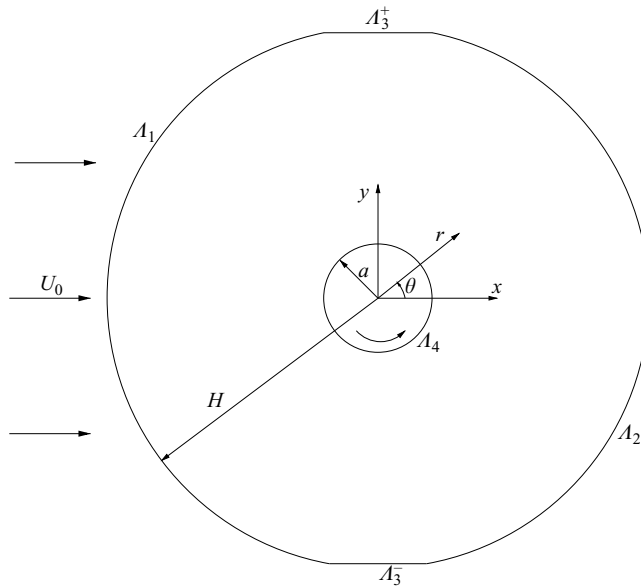
FIGURE 1. Scheme of the computational domain showing the Cartesian and polar reference coordinate systems. The boundary conditions correspond to: Λ_1, inflow; Λ_2, outflow; Λ_3, zero-shear stress boundaries, and Λ_4, wall with prescribed velocity and no-slip condition.

to that adopted by Kang *et al.* (1999). Other mesh types reported in the literature are the C-type mesh referred to by Kang *et al.* (1999) and the square-type mesh used by Mittal & Kumar (2003) in their finite-elements computations. An O-type mesh is expected to save computational effort as compared with a C-type mesh or a square mesh with sides of length H/a. In this study, the domain is partially delimited by two arcs of a circle, one upstream of the cylinder and the other one downstream, and both have the same radius H. The dimensionless radii of the upstream and downstream arcs are determined as $\tilde{H} \equiv H/2a$.

The boundary conditions applied in this investigation can be described as follows. The left-hand arc Λ_1 (figure 1) is the inflow section or upstream section, where a Dirichlet-type boundary condition for the Cartesian velocity components, $\tilde{u} = 1$ and $\tilde{v} = 0$ is prescribed, i.e. the free-stream velocity is imposed. The right-hand arc Λ_2 represents the outflow boundary, where it is considered that the diffusion flux in the direction normal to the exit surface is zero for all variables. Therefore, extrapolation from inside the computational domain is used to compute the flow variables at the outflow plane, which do not influence the upstream conditions (see Fluent® 6.1's User's Guide for details about the numerical schemes and boundary conditions used by the package). On the straight horizontal segments Λ_3^+ and Λ_3^-, a zero normal velocity and a zero normal gradient of all variables are prescribed. As a consequence, a zero shear stress condition is imposed at these two boundaries. These relatively short segments are two chords in a circle of radius H, parallel to the horizontal x-axis and are symmetric with respect to the vertical y-axis. The sectors of the circle that contain these segments have a span of 10° each. The inclusion of these segments defines a transition region between the inlet and outlet sections, and can be thought to be the adaptation to an O-type mesh of the zero-shear-stress upper and lower boundaries, parallel to the free stream, that Mittal & Kumar (2003) used in their

domain. Finally, the dimensionless pheripheral or tangential velocity $\tilde{q}$ is prescribed on the surface of the rotating cylinder along with a no-slip boundary condition. The cylinder rotates in the counterclockwise direction.

As initial condition in this numerical investigation, the values given to the velocity components at the inflow section are extended over the interior of the computational domain. Since we are focused on the fully developed flow, as Kang *et al.* (1999) pointed out, the simulations may be started with arbitrary initial conditions. They performed a numerical study with different initial conditions, including the impulsive start-up, for $Re = 100$ and $\tilde{q} = 1.0$ and the same fully developed response of the flow motion was eventually reached in all cases. In contrast, solving the steady version of the Navier–Stokes equations may yield multiple numerical solutions, depending on the given Re and $\tilde{q}$ and the initial guess used to start the computations, as was demonstrated from simulations carried out by Mittal & Kumar (2003). Keeping the unsteady term in the equations of motion prevents the occurrence of unrealistic predictions and permits us to acknowledge and describe the unsteady behaviour, which is a major feature of the process of vortex shedding, when it occurs. For instance, Tang & Ingham (1991) dropped the unsteady term of the Navier–Stokes equations and found steady-state solutions for $Re = 60$ and 100 and $0 \leqslant \tilde{q} \leqslant 1$ where experimental and numerical evidence indicates that unsteady periodic flow takes place (e.g. Kang *et al.* 1999). The study of fully developed flows, where a periodic unsteady state prevails, lies beyond the scope of this work. Here, the numerical experiments are focused on the steady state (i.e. fully developed non-periodic) flow motion.

In order to find a suitable position for the outer boundary, such that it appropriately approximates the real condition far from the surface of the rotating cylinder, different values of the $\tilde{H}$ parameter are considered ranging from 50 to 175 with increments of 25 units. For these grid sizes, a numerical study is performed for $Re = 400$ and $\tilde{q} = 5$ and $Re = 1000$ and $\tilde{q} = 3$ to determine the variation of the lift, drag and torque coefficients with the parameter $\tilde{H}$ (figure 2). From this figure, it is clear that beyond $\tilde{H} = 75$ the coefficients show an asymptotic behaviour; then, $\tilde{H} = 125$ is selected as the fixed radial position of the upstream and downstream arcs of the circular outer boundary. This analysis is carried out with a dimensionless time step of $\Delta\tilde{t} = 0.02$. This time step was chosen in agreement with Kang *et al.* (1999), while Mittal & Kumar (2003) used a dimensionless time step of 0.0125. Since the segregated method selected from the solver is implicit, no dependency on the time step occurs in terms of numerical stability. With respect to the spatial step size, we assign the value recommended by Mittal & Kumar (2003) for the thickness or radial step size of the first layer of cells (i.e. cells attached to the wall), $\tilde{h}_a = 0.0025$. A very fine mesh is used around the cylinder, with the size of the cells gradually increasing as the distance from the wall becomes larger. Following the approach of Chew *et al.* (1995), a rough calculation using the Blasius solution for the boundary-layer thickness $\tilde{\delta}$ for flow past a flat plate, but with the Reynolds number based on the peripheral velocity of the cylinder (i.e. $\tilde{\delta} \sim (\pi/\tilde{q}Re)^{1/2}$) indicates that this choice of the radial-spatial step size provides a good resolution of the boundary-layer thickness. Table 1 gives the parameters defining the various meshes considered in this analysis; N_a is the number of nodes in the circumferential direction. Tests of the sensitivity of simulation results to mesh refinement were carried out using the meshes designated as M125 (lower $\Delta\tilde{t}$) and M125b in table 1 for $Re = 400$ and $\tilde{q} = 5$ and $Re = 1000$ and $\tilde{q} = 3$. The lift and torque coefficients do not change much under mesh refinement, but the drag coefficient does change. The changes in the drag coefficient seem relatively large because the coefficients are small, one or more orders of magnitude lower than the
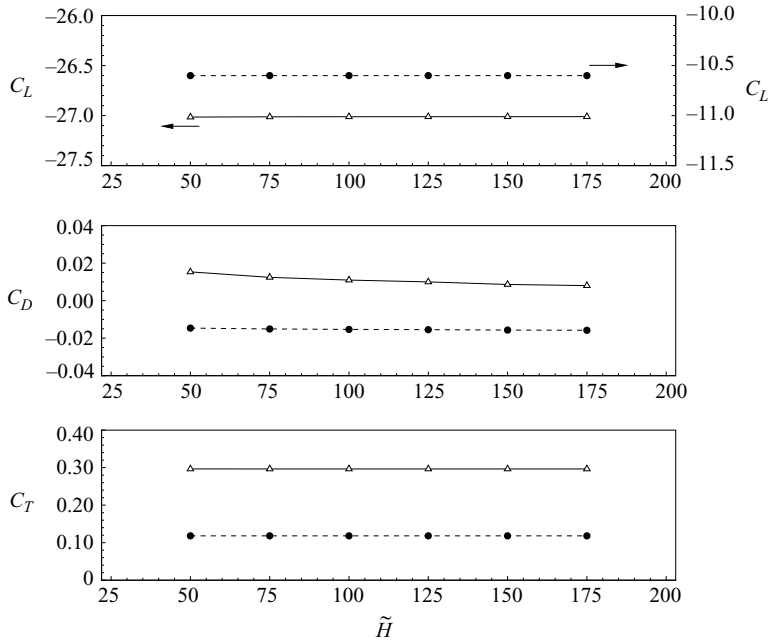
FIGURE 2. Influence of the dimensionless position of the outer boundaries (inlet and outlet) $\tilde{H}$ on the lift, drag and torque coefficients for $Re = 400$ and $\tilde{q} = 5.0$ (solid line with $\triangle$) and $Re = 1000$ and $\tilde{q} = 3.0$ (dashed line with $\bullet$).

Mesh	Nodes	Cells	N_a	$\tilde{H}$	$\tilde{h}_a$ ($\times 10^{-3}$)	$\Delta \tilde{t}$
M50	22 080	21 920	160	50	2.50	0.02
M75	24 160	24 000	160	75	2.50	0.02
M100	25 760	25 600	160	100	2.50	0.02
M125	26 880	26 720	160	125	2.50	0.01/0.02
M150	28 000	27 840	160	150	2.50	0.02
M175	29 120	28 960	160	175	2.50	0.02
M125b	50 820	50 600	220	125	1.25	0.01

TABLE 1. Properties of the meshes considered in the numerical simulations.

lift and torque coefficients (see tables 4 and 9). This issue is also addressed in the next section. As a result of this systematic study, the mesh M125 from table 1 with $\Delta \tilde{t} = 0.02$ was selected for our numerical experiments. All the results presented in the forthcoming sections are computed using this mesh and time step. Figure 3 shows the structure of a typical mesh (for $\tilde{H} = 125$, mesh M125) which is more refined near the wall.

3. Results and dicussion

In this section, we present the numerical results for streaming flow past a rotating circular cylinder for various Re and $\tilde{q}$. First, we validate our numerical set-up by comparing results for selected cases with those from a previous publication. Then, the streamlines and vorticity contours are plotted and discussed. Next, the shape and extension of the vortical region around the rotating cylinder is addressed based on
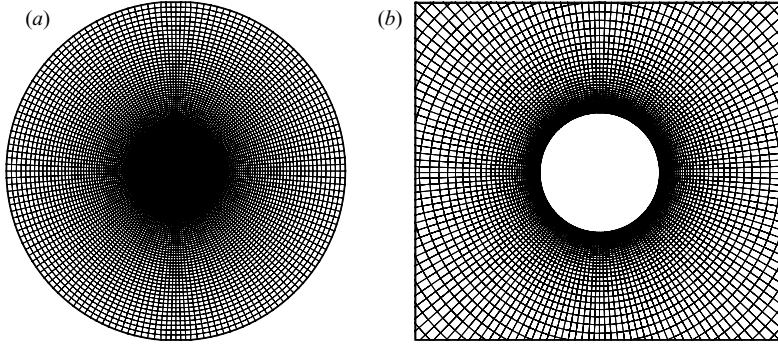
FIGURE 3. O-type mesh used in the numerical simulations (M125). (*a*) Extended mesh. (*b*) Close-up of the mesh around the cylinder.

the vorticity field obtained from the numerical experiments. The prediction of the outer edge of the vortical region is accomplished imposing a cutoff value such that the magnitude of the vorticity at this position approximates this critical value. The outermost curve that satisfies this criterion is found. We also present the drag and lift coefficients on the rotating cylinder as computed from the numerical simulations. Since different positions of the outer edge of the vortical region can be obtained by simply prescribing a different (and still reasonable) cutoff value, two alternative effective values of the thickness of the vortical region are proposed for every pair of Re and $\tilde{q}$ based on the agreement between the theoretical predictions by WJa and the numerical results. The first effective thickness comes from matching the pressure drag at the edge of the vortical region proposed by WJa with the corresponding numerical profile, whereas the second effective thickness results from matching WJa's pressure lift on the surface of the cylinder with the respective numerical value. Each of these two values of the effective vortical region thickness is used to compute various parameters relevant to this type of fluid motion. For some of these parameters, predictions from the theoretical approaches of Glauert (1957) and WJa are presented for comparison.

3.1. *Validation of the numerical approach*

The first step is to validate the problem set-up, the choice of numerical methods and mesh attributes by comparing results from our numerical simulations with results obtained from the literature, provided the same conditions are imposed. This comparison is performed with the numerical results of Mittal & Kumar (2003) for $Re = 200$ with $\tilde{q} = 4$ and 5 under the steady-state condition. The outcomes included in the comparison are the lift and drag coefficients as defined in (2.4) as well as the dimensionless vorticity and pressure coefficient on the surface of the rotating circular cylinder. The dimensionless form of the vorticity is $\tilde{\omega} = 2a\omega/U_0$, while the pressure coefficient is defined as:

$$c_p = \frac{p - p_\infty}{\frac{1}{2}\rho U_0^2}, \tag{3.1}$$

where p_∞ represents the pressure as the radial coordinate r goes to infinity and p represents the pressure on the surface of the circular cylinder. In the numerical simulations, the reference pressure p_∞ is taken to be zero at the point where the axis $y = 0$ intercepts the upstream boundary. In our simulations, it is verified that the pressure tends closely to zero everywhere along the outer boundary of the domain.

		Present study		Mittal & Kumar	
Re	$\tilde{q}$	C_L	C_D	C_L	C_D
200	3	−10.3400	0.0123	−10.3660	0.0350
200	4	−17.5820	−0.1240	−17.5980	−0.0550
200	5	−27.0287	0.0107	−27.0550	0.1680

TABLE 2. Comparison between the lift and drag coefficients acting on the surface of the rotating cylinder, C_L and C_D, computed in the present study with the results of Mittal & Kumar (2003).
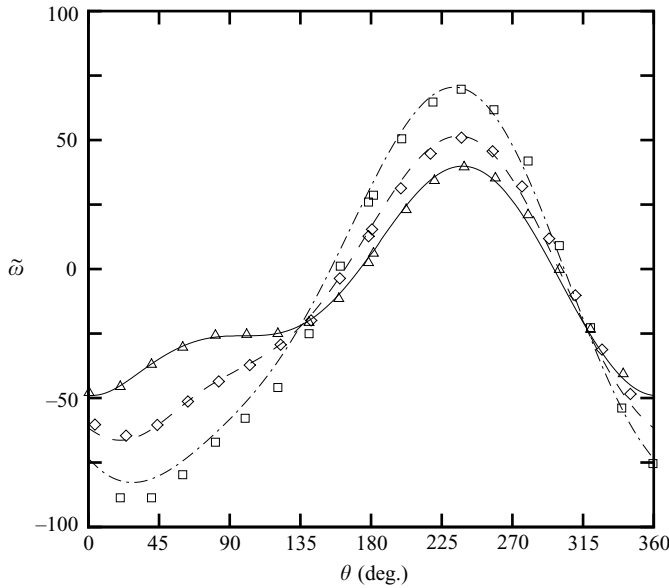

FIGURE 4. Dimensionless vorticity profiles on the surface of the rotating cylinder for $Re = 200$. Present computations: solid line, $\tilde{q} = 3$; dashed line, $\tilde{q} = 4$; dash-dotted line, $\tilde{q} = 5$. Results of Mittal & Kumar (2003): △, $\tilde{q} = 3$; ◇, $\tilde{q} = 4$; □, $\tilde{q} = 5$.

This result prevails since the free-stream conditions are approached on the outer boundary.

Table 2 compares the lift and drag coefficients computed here with values given by Mittal & Kumar (2003). We have already noted that the agreement for the lift coefficient is good, but discrepancies in the values of the drag coefficient are larger; the drag coefficients are so small that the relative errors are magnified. Figures 4 and 5 show that the dimensionless vorticity and pressure coefficient for $Re = 200$ with $\tilde{q} = 4$ and 5 are in good agreement with slightly less good agreement for $Re = 200$ and $\tilde{q} = 5$ where the pressure coefficient on the upper surface of the cylinder ($0° \leqslant \theta \leqslant 180°$) is slightly disturbed. This behaviour may be related to the differences between our results and those of Mittal & Kumar for the drag coefficient. The pressure distribution around the surface of the cylinder contributes to the drag and the larger discrepancies are evident at large values of $\tilde{q}$. For the largest value of $\tilde{q}$ ($= 5$) the differences in the computational strategies used here and by Mittal & Kumar (2003) in terms of mesh shape and numerical schemes are most evident in the values of the drag. We do not know which computational approach is more accurate.
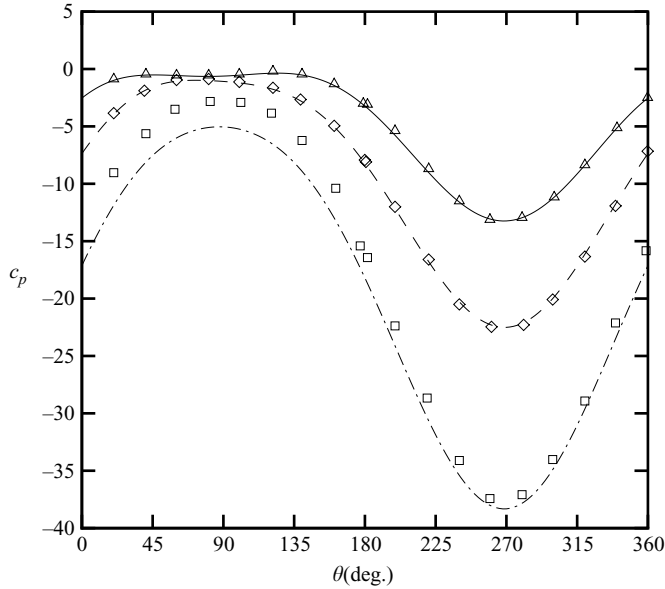
FIGURE 5. Pressure coefficient profiles on the surface of the rotating cylinder for $Re = 200$. Present computations: solid line, $\tilde{q} = 3$; dashed line, $\tilde{q} = 4$; dash-dotted line, $\tilde{q} = 5$. Results of Mittal & Kumar (2003): $\triangle$, $\tilde{q} = 3$; $\diamond$, $\tilde{q} = 4$; $\square$, $\tilde{q} = 5$.

We have also solved the steady-state Navier–Stokes equations for the cases of $Re = 200$ with $\tilde{q} = 4$ and 5. The former case produces a stable solution that converges to the same values obtained with the unsteady version of the equations of motion. In contrast, the latter case does not converge to steady state. Mittal & Kumar (2003) showed through a global non-parallel stability analysis of the solutions of the steady-state Navier–Stokes equations that, depending on the initial guess, instability of the solutions with respect to small disturbances occur for $\tilde{q} \geqslant 4.8$ when $Re = 200$. Hence, multiple solutions take place in this region. In our computations, we monitor the trends of the lift, drag and momentum coefficients as functions of time to determine the convergence of the solution to steady state.

3.2. *Vortical region thickness from the numerical flow field*

After the evaluation of the numerical set-up with results from the literature have been accomplished, we compute the flow field for flow past a rotating circular cylinder for $Re = 400$ with $\tilde{q} = 4$, $\tilde{q} = 5$ and $\tilde{q} = 6$ and for $Re = 1000$ and $\tilde{q} = 3$. In addition, the computations for $Re = 200$ with $\tilde{q} = 4$ and $\tilde{q} = 5$, already used for comparison with results presented in a previous publication, are also included in this data set. The choice of this set of Reynolds number Re and peripheral speed $\tilde{q}$ for the numerical simulations renders a gentle convergence to steady-state fully developed flow when the unsteady incompressible Navier–Stokes equations are solved. For flow past a rotating circular cylinder, the boundary layer remains attached to the surface of the cylinder if the dimensionless peripheral velocity $\tilde{q}$ lies beyond a certain threshold so that separation is avoided and vortex shedding is suppressed. As mentioned above, this critical value of $\tilde{q}$ is a function of Re. Furthermore, the selected range of parameters Re and $\tilde{q}$ is likely to avoid large inertia effects that yield transition to turbulence and three-dimensional effects. A reasonable assumption, based on literature review and
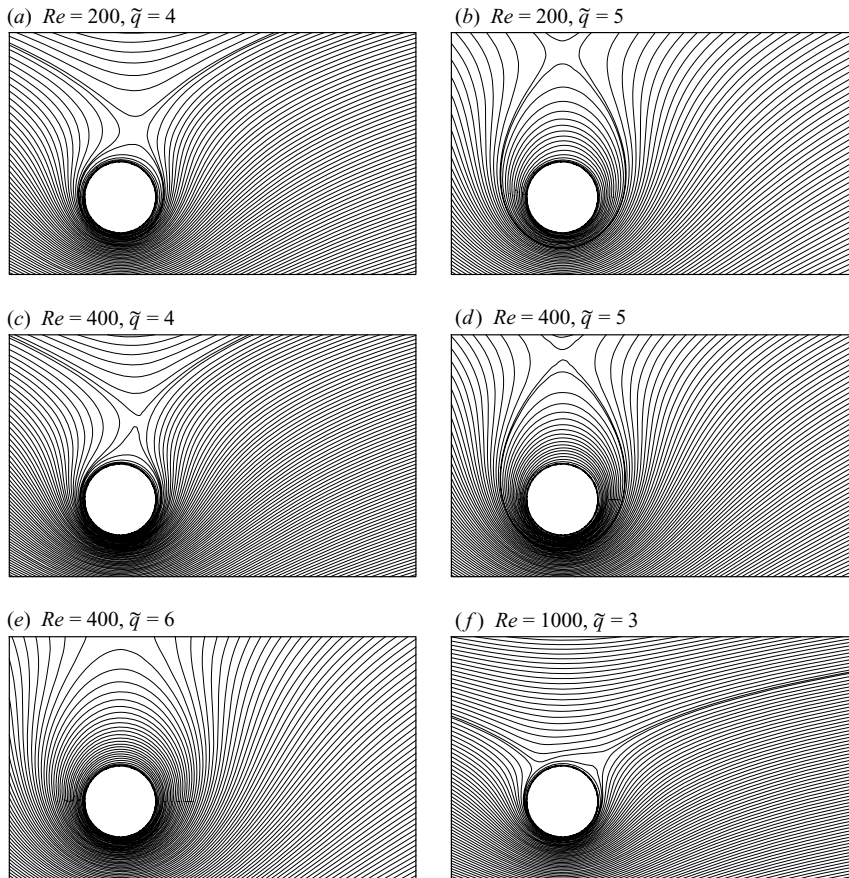
(*a*) *Re* = 200, $\tilde{q}$ = 4   (*b*) *Re* = 200, $\tilde{q}$ = 5

(*c*) *Re* = 400, $\tilde{q}$ = 4   (*d*) *Re* = 400, $\tilde{q}$ = 5

(*e*) *Re* = 400, $\tilde{q}$ = 6   (*f*) *Re* = 1000, $\tilde{q}$ = 3

FIGURE 6. Streamlines for various pairs of *Re* and $\tilde{q}$. The rotation of the cylinder is counterclockwise while the streaming flow is from left to right. The stagnation point lies above the cylinder. The stagnation point moves upwards as the peripheral speed $\tilde{q}$ increases for a fixed *Re*.

previous computations (Chew *et al.* 1995), indicates taking $\tilde{q} \leqslant 6$ as a limiting value. However, this upper limit may be expected to be also a function of *Re*.

Figure 6 shows the streamline patterns for the various pairs of *Re* and $\tilde{q}$ considered in this investigation. Notice that the stagnation point lies above the cylinder, in the region where the direction of the free stream opposes the motion induced by the rotating cylinder. As the dimensionless peripheral speed at the surface of the cylinder increases, for a fixed *Re*, the region of close streamlines around the cylinder extends far from the wall and, as a consequence, the stagnation point moves upwards. For the lowest $\tilde{q} = 3$, the region of close streamlines becomes narrow and the stagnation point lies near the upper surface of the cylinder. The contours of positive and negative vorticity are presented in figure 7. The positive vorticity is generated mostly in the lower half of the surface of the cylinder while the negative vorticity is generated mostly in the upper half. For the dimensionless peripheral speeds of $\tilde{q} = 3$ and 4, a zone of relatively high vorticity stretches out beyond the region neighbouring the rotating cylinder for $0° \leqslant \theta \leqslant 90°$, resembling 'tongues' of vorticity. Increasing $\tilde{q}$, the rotating cylinder drags the vorticity so the 'tongues' disappear and the contours of positive and negative vorticity appear wrapped around each other within a narrow
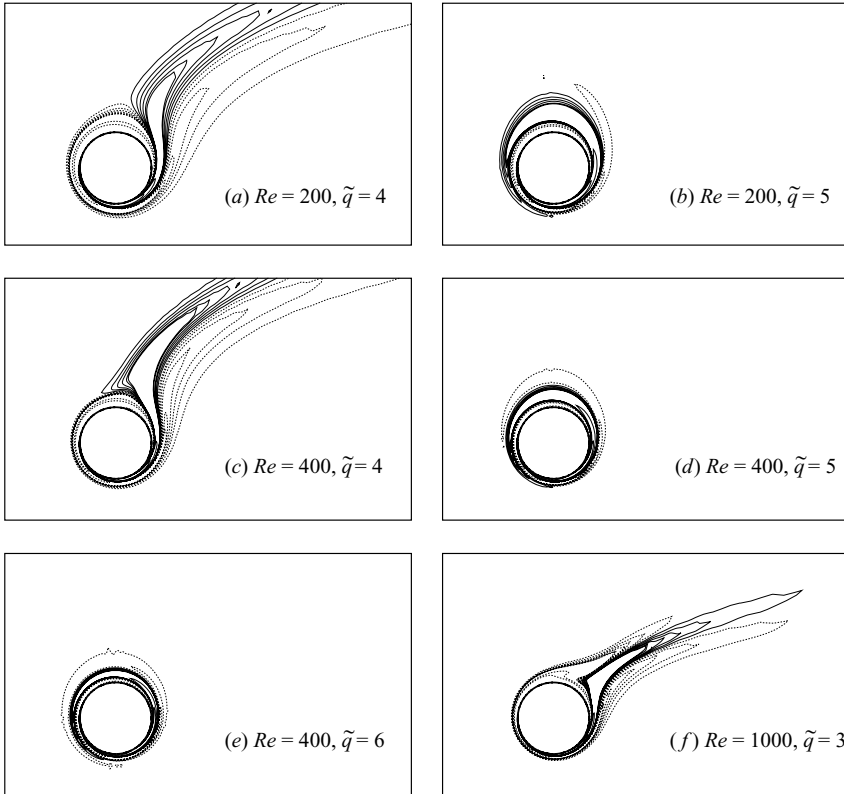
FIGURE 7. Vorticity contours for various pairs of Re and $\tilde{q}$. The negative vorticity is shown as dashed lines. The rotation of the cylinder is counterclockwise while the streaming flow is from left to right.

region close to the surface. Based on the velocity and pressure fields obtained from the simulations for the various Re and $\tilde{q}$ considered, the next step in this numerical study is to identify the region where the vorticity effects are mostly confined. In a classical sense, the term boundary layer has been reserved for a narrow or thin region, attached to a solid surface, where the vorticity is non-negligible. The concept of a boundary layer attached to a wall is linked to the idea of potential flow. Once the boundary layer has been delimited, the analysis follows by applying the relatively simple, but still powerful, theory of potential flow to approximate the external fluid motion. Nevertheless, this approximation may become inadequate when separation occurs. For flow past a stationary cylinder, separation is present near the downstream end of the cylinder even at Re as low as 5 (Panton 1984). In contrast, for flow past a rapidly rotating cylinder, the separation of the boundary layer can be suppressed for a critical $\tilde{q}$ given Re. The Reynolds number based on the free-stream velocity also plays an important role in the boundary-layer analysis. In this investigation, a more general term, vortical region, is used to designate the region where the effects of viscosity are mostly restricted. The vortical region may extend relatively far from the surface where it is attached in opposition to the thinness implied in the classical boundary-layer concept. A boundary layer is certainly a vortical region; however, a relatively thick vortical region may or may not be regarded as a boundary layer.

For the type of fluid motion considered in this investigation, the vortical region lies in the fluid zone enclosed between the surface of the rotating circular cylinder and a contour surrounding this solid cylinder, named the outer edge of the vortical region. Beyond this surface, the effect of vorticity is regarded as negligible. As a first approximation, we propose that the radial position of the outer edge of the vortical region is determined such that, for a given angular position, the vorticity magnitude is approximately 1% of the maximum value of the vorticity magnitude field. This *ad hoc* 1% criterion is then applied to a set of discrete angular positions around the rotating cylinder ($0° \leqslant \theta \leqslant 360°$), with a constant incremental angular step, using the flow field obtained from the numerical simulations. Therefore, the radial position of the outer edge of the vortical region as a discrete function of the azimuthal coordinate θ can be determined for every pair of Re and $\tilde{q}$. Since the 1% of the maximum vorticity magnitude criterion may be satisfied at multiple radial positions, for any given azimuthal position, the point with the largest $\tilde{r}$ among them is chosen to determine the outer edge of the vortical region. The radial position of the outer edge of the vortical region as a function of θ determines a non-constant thickness of the vortical region. Hence, a profile of this thickness as a function of the angular position can be generated.

For practical reasons, it is convenient to deal with a constant value of the radial position of the outer edge of the vortical region and then with a constant vortical region thickness. To find this uniform value, $\tilde{r}_\delta$, a straightforward choice is the average of the discrete set of radial positions that defined the edge of the vortical region as a function of θ from the previous methodology. Then, a uniform vortical region thickness, $\delta_{1\%}/a$, expressed in dimensionless fashion, is easily computed from the simple geometric formula:

$$\delta_{1\%}/a = 2\tilde{r}_\delta - 1. \tag{3.2}$$

Figure 8 shows the thickness of the vortical region as a function of the azimuthal coordinate as well as its average value for different pairs of Re and $\tilde{q}$. In all the cases considered, the vortical region is thick in the upper half of the cylinder ($0° \leqslant \theta \leqslant 180°$), where the fluid is retarded and the viscous effects are emphasized, while its thickness decreases in the lower half ($180° \leqslant \theta \leqslant 360°$), where the fluid is accelerated. For $Re = 200$ and 400 and $\tilde{q} = 4$ and $Re = 1000$ and $\tilde{q} = 3$, the graphs show a prominent peak in the region $45° \leqslant \theta \leqslant 90°$. This trend indicates that a region of vorticity magnitude higher than 1% of the maximum vorticity magnitude in the whole domain lies relatively far from the wall. For $Re = 200$ and $\tilde{q} = 5$ and $Re = 400$ and $\tilde{q} = 5$ and 6, the peak is replaced by a hump that reaches its maximum by $\theta = 90°$. This result indicates that the region of high vorticity has been wrapped around the cylinder as a consequence of the higher rotational speed. This is verified in figure 7. In addition, the constant radial position of the vortical region edge $\tilde{r}_\delta$ and its corresponding vortical region thickness $\delta_{1\%}/a$ for various Re and $\tilde{q}$ are given in table 3. These results reveal that the vortical region thickness is far from negligible for all the cases. Moreover, it is shown in table 3 that, as $\tilde{q}$ increases for a fixed Re, the average vortical region thickness $\delta_{1\%}/a$ decreases. By increasing the rotational speed of the cylinder, the local Reynolds number near its wall also increases and the inertia effects then become even more dominant than the viscosity effects, which turn out to be confined to a smaller region. A similar reasoning applies to the trend observed for a fixed $\tilde{q}$, where $\delta_{1\%}/a$ decreases as Re increases.

The outer edge of the vortical region from the 1% criterion as a function of the angular position θ for various pairs of Re and $\tilde{q}$ is presented in figure 9 along with
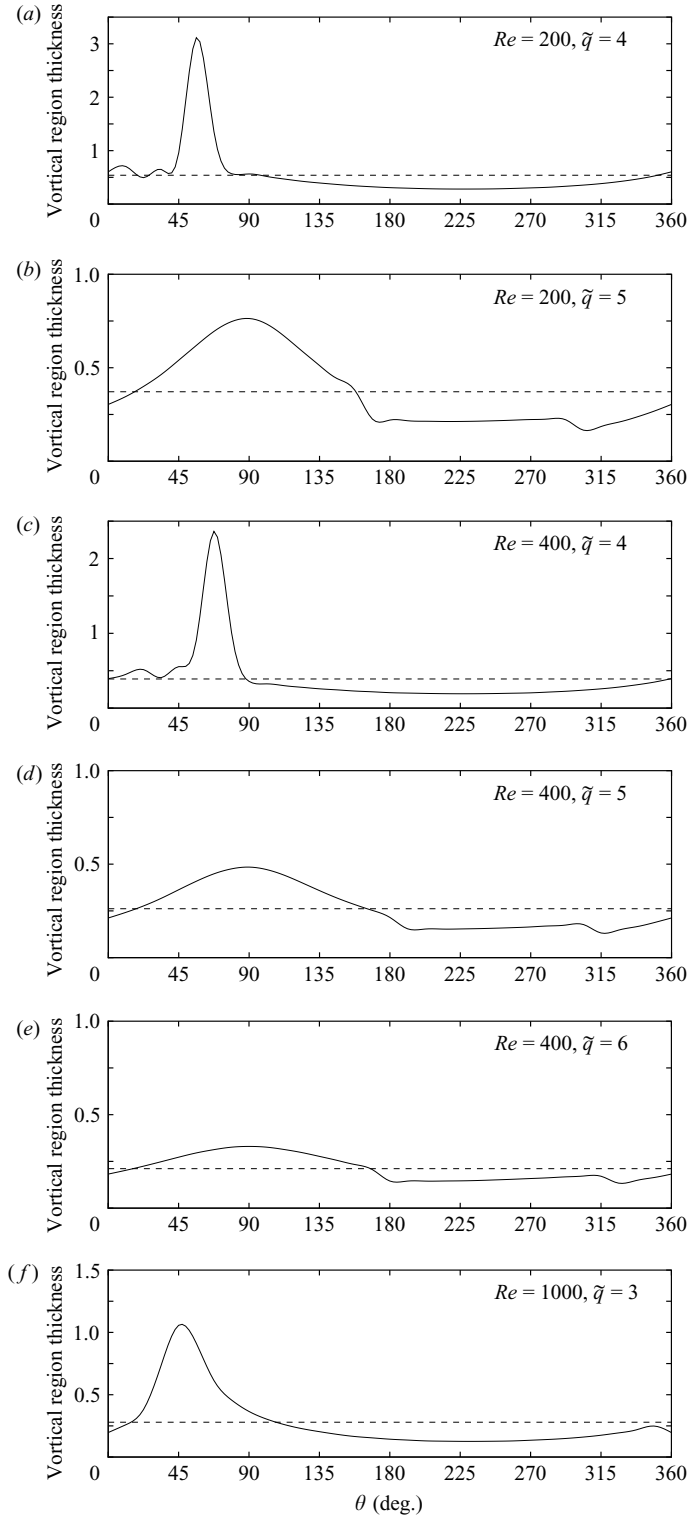
FIGURE 8. Variable vortical region thickness as a function of the angular position θ (solid line) for various pairs of Re and $\tilde{q}$ obtained applying the 1% criterion. In addition, the uniform vortical region thickness $\delta_{1\%}/a$ (dashed line) computed as the average of the profile is included.

Re	$\tilde{q}$	$\tilde{r}_\delta$	$\delta_{1\%}/a$
200	4	0.771	0.541
200	5	0.685	0.369
400	4	0.695	0.390
400	5	0.630	0.260
400	6	0.605	0.210
1000	3	0.638	0.277

TABLE 3. Radial position of the outer edge of the vortical region $\tilde{r}_\delta$ and thickness of the vortical region $\delta_{1\%}/a$ based on the 1% of the maximum vorticity magnitude criterion for various pairs of Re and $\tilde{q}$.
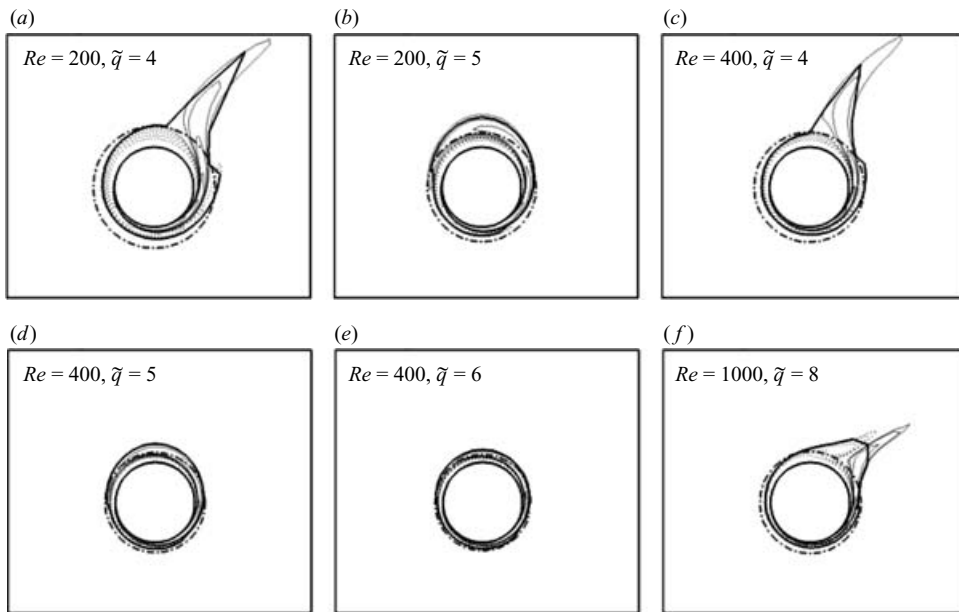

FIGURE 9. Position of the outer edge of the vortical region based on the 1% criterion. The thick-solid line represents the edge of the vortical region with variable thickness. The thick dash-dotted line represents the edge of the vortical region with uniform thickness $\delta_{1\%}/a$. The thin-solid lines represent contours of positive vorticity while the thin-dashed lines represent contours of negative vorticity. The contours show only levels of vorticity with magnitude greater than or equal to 1% of the maximum vorticity magnitude in the fluid domain. The rotation of the cylinder is counterclockwise while the streaming flow is from left to right.

the vorticity contours. The corresponding outer edge of the vortical region for a uniform thickness $\delta_{1\%}/a$ is also included. Only levels of vorticity whose magnitude is greater than or equal to 1% of the maximum vorticity magnitude in the fluid domain are shown. Since the position of the outer edge of the vortical region is obtained from a discrete set of angular positions, short sections of some iso-vorticity lines may lie outside the non-constant thickness vortical region. The large spikes presented in figure 8 are also represented here, corresponding to the regions of vorticity magnitude greater than 1% that extend far from the cylinder in the interval $0° \leqslant \theta \leqslant 90°$.

It is recognized that the criterion set to define the outer edge of the vortical region is somewhat arbitrary. A new reasonable cutoff value can be prescribed and

Re	$\tilde{q}$	C_L	C_{L_p}	C_{L_f}	C_D	C_{D_p}	C_{D_f}
200	4	−17.5820	−16.9612	−0.6208	−0.1240	−0.7278	0.6038
200	5	−27.0287	−26.1826	−0.8460	0.0107	−0.8245	0.8352
400	4	−18.0567	−17.6095	−0.4472	−0.0836	−0.5341	0.4505
400	5	−27.0112	−26.4147	−0.5965	0.0100	−0.5912	0.6012
400	6	−33.7691	−33.0868	−0.6823	0.0136	−0.6677	0.6813
1000	3	−10.6005	−10.4085	−0.1920	−0.0155	−0.2129	0.1974

TABLE 4. Numerical results for the lift and drag coefficients, C_L and C_D, corresponding to the forces acting on the cylinder. The decomposition of these values in their corresponding components from pressure (C_{L_p} and C_{D_p}) and viscous shear stress (C_{L_f} and C_{D_f}) are included.

substantial differences may be found in terms of the position of the outer edge of the vortical region, its thickness and its shape. Here, this preliminary criterion has been introduced to show that a region can be delimited where the effects of vorticity are circumscribed. This region is found to be attached to the rotating cylinder and its outer edge varies with the polar angle, for a sufficiently large rotational speed. In forthcoming sections, we motivate and establish new conditions that prescribe the thickness of the vortical region founded on the agreement between theoretical predictions and numerical results.

3.3. *Drag and lift coefficients and pressure distribution from the numerical solution*

The analysis of the forces that the fluid motion produces on the rotating cylinder has been a topic of major importance in aerodynamics. For streaming flow past a rotating cylinder, these forces have usually been presented in terms of two mutually perpendicular components, a component aligned with the free-stream velocity vector, the drag force, and a component perpendicular to this direction, the lift force. In addition, the rotation of the cylinder induces a torque with respect to its centre that deserves attention. It is also customary to express these forces and torque in dimensionless form as coefficients. The form for the drag, lift and torque coefficients adopted in this work were presented in (2.4). The results and discussion for the torque coefficient will be given in a later section.

The numerical results for the total lift and drag coefficients corresponding to the forces that the fluid motion produces on the rotating circular cylinder are presented in table 4. The contributions to these values from the pressure and the viscous shear stress are shown as well. The results for $Re = 200$ and $\tilde{q} = 4$ and 5 from table 2 are included for completeness. The results in table 4 indicate that the pressure lift coefficient C_{L_p} represents by far the largest contribution to the total lift C_L, in comparison with the shear stress lift coefficient C_{L_f}. The pressure and shear stress components of the lift force have the same direction as the total lift force, pointing toward the negative direction of the y-axis in the current reference frame. By contrast, the pressure drag coefficient C_{D_p} and the shear stress drag coefficient C_{D_f} show a similar order of magnitude; however, these components of the total drag force point in opposite directions, with the pressure drag force pointing toward the upstream boundary (i.e. opposite to the direction of the free-stream velocity). The net effect of the pressure and shear stress drag is a relatively small total drag coefficient whose magnitude is, in all the cases considered, within 1% of the magnitude of the total lift coefficient. For a constant value of Re, by increasing the peripheral velocity $\tilde{q}$

the magnitude of the total lift coefficient, as well as the pressure and shear stress lift coefficients increase. The same trend is observed with the magnitude of the pressure and shear stress drag coefficients. By keeping $\tilde{q}$ constant, the increase of Re yields an increase of the magnitude of the pressure lift coefficient, but a decrease in the magnitude of the shear stress components of the lift and drag and the pressure drag coefficients. It is also of interest to observe and analyse the trend followed by the pressure distribution in the fluid domain, especially in the neighbourhood of the rotating cylinder. Figure 10 shows the profiles of the pressure coefficient c_p as defined in (3.1) as a function of the radial coordinate for various Re and $\tilde{q}$. For every pair of Re and $\tilde{q}$, the c_p profiles for different angular positions are presented. The pressure coefficient has been computed from the pressure field obtained from the numerical simulations. The pressure coefficient as a result of the exact solution of the equations of motion for purely rotary flow due to the spinning cylinder embedded in an infinite fluid domain is presented as a reference level. The corresponding expression is

$$c_p = -\frac{\tilde{q}^2}{4\tilde{r}^2}, \tag{3.3}$$

independent of the angular position θ. In all the cases considered, this solution for c_p always lies inside the extreme profiles corresponding to $\theta = 90°$ and $\theta = 270°$. The graphs demonstrate that the pressure coefficient changes strongly near the wall, inside the vortical region, resembling the tendency described by the purely rotary flow solution, while becoming flat and tending slowly to zero as the radial coordinate $\tilde{r}$ approaches the outer boundaries. For a fixed peripheral speed $\tilde{q}$, it is observed that increasing Re has little effect on the pressure coefficient profiles. In contrast, for a fixed Re, increasing $\tilde{q}$ expands the range of values that the pressure coefficient takes for a given radial position. For instance, this trend can be monitored on the surface of the rotating cylinder, $\tilde{r} = 0.5$, and at the outer edge of the vortical region, $\tilde{r} = \tilde{r}_\delta$, in figure 10. This tendency may be addressed in the frame of the irrotational flow theory. The expression for the pressure coefficient distribution for potential flow past a circular cylinder with circulation (dimensionless) $\tilde{\Gamma}$ $(= \Gamma/2aU_0)$ is recalled here:

$$c_p = \frac{\cos 2\theta}{2\tilde{r}^2} - \frac{1}{16\tilde{r}^4} - \frac{\tilde{\Gamma}^2}{4\pi^2\tilde{r}^2} + \frac{\tilde{\Gamma}}{\pi}\sin\theta\left(\frac{1}{\tilde{r}} + \frac{1}{4\tilde{r}^3}\right). \tag{3.4}$$

It is clear from this expression that, for a fixed radial position, the amplitude of the $(\sin\theta)$ term increases when the circulation increases. Also, this theory predicts the decrease of the mean value of c_p when the circulation rises. It will be shown later that the circulation increases when the peripheral speed $\tilde{q}$ increases. The tendencies described by the classical irrotational theory for the pressure coefficient distribution are followed by the numerical solution obtained in this investigation.

3.4. *Effective vortical region thickness from the viscous correction of viscous potential flow*

The results from the numerical experiments carried out in this investigation as well as from previous publications represent reliable information that can be used to evaluate the prediction capabilities of theoretical approaches. In addition, theoretical models can be used to achieve a better understanding of the numerical results and to extract relevant information from the computations, which is not evident at first sight. For these purposes, we focus on the work of WJa, who introduced a simple modification of the boundary-layer solution proposed by Glauert (1957) to find new expressions
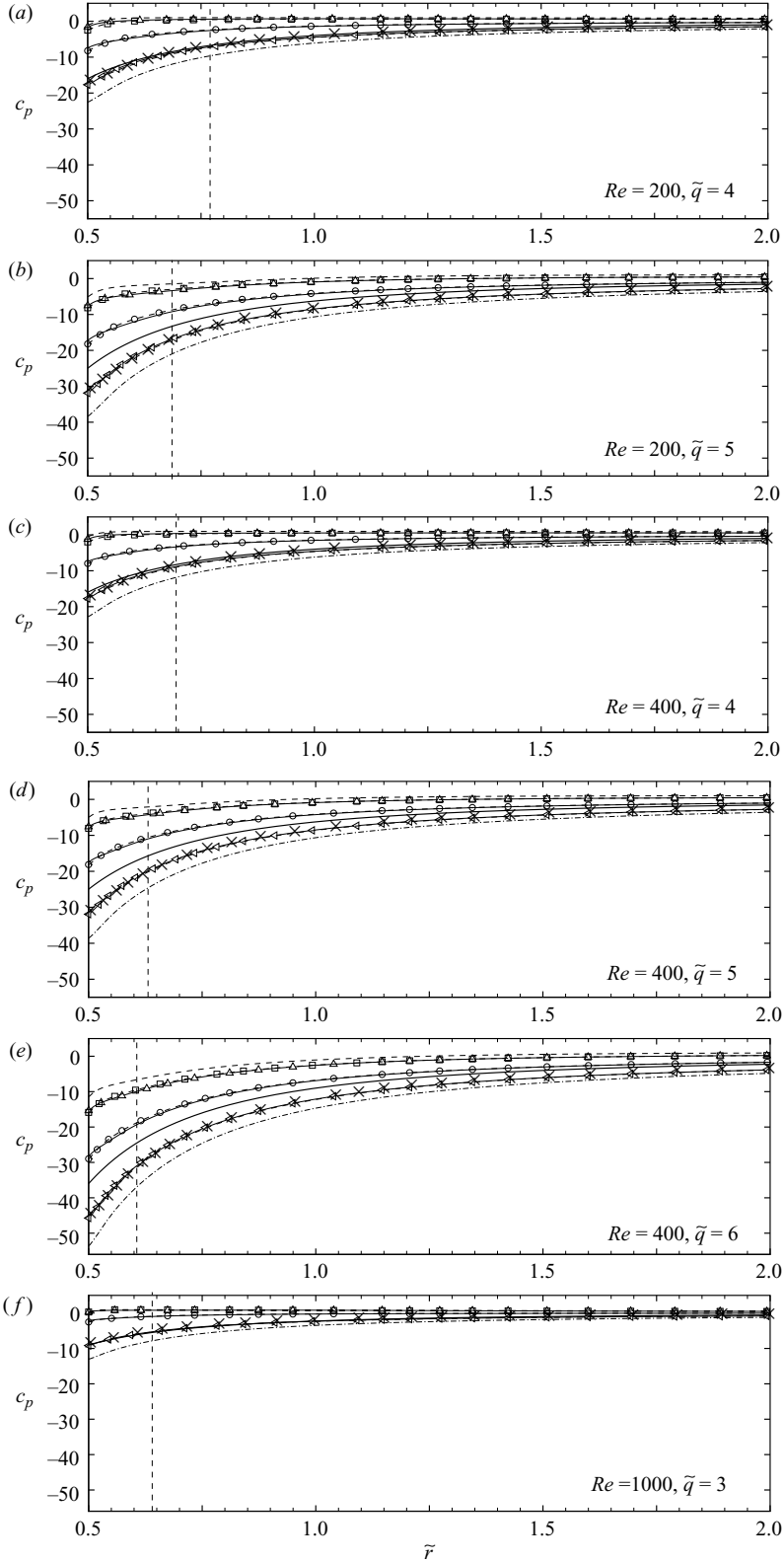
FIGURE 10. For caption see facing page.

for the pressure lift and torque on the cylinder and also applied their VCVPF theory to find an expression for the pressure drag at the outer edge of the vortical region.

The viscous correction of viscous potential flow (VCVPF) theory adds an extra-pressure term to the irrotational pressure at the edge of the boundary layer to compensate the irrotational shear stress. Outside the boundary layer, the irrotational flow of a viscous fluid is considered. WJa's pressure correction is a 2π-periodic function on a circle; they proposed to expand this pressure correction as a Fourier series. They found an expression for the coefficient of the $\cos\theta$ term of the Fourier series using the VCVPF theory. The Fourier series expansion for the pressure correction can be inserted in the definition of the drag due to pressure that the fluid outside the vortical region produces on the outer edge of this zone. Then, an expression for the drag due to pressure can be obtained as a function of the coefficient of the $\cos\theta$ term of the Fourier series. A brief review of this procedure is presented next.

The total drag force can be decomposed into its pressure and viscous shear stress components. Let D_p denote the component of the drag force due to pressure. From (2.3) and (2.4), we can express D_p as a drag coefficient:

$$C_{D_p} = \frac{D_p}{\rho U_0^2 a}. \tag{3.5}$$

The pressure drag can be determined with direct integration from the pressure distribution. Then, using (3.5), the pressure drag coefficient can be written as

$$C_{D_p} = -\int_0^{2\pi} 2\,\tilde{p}\cos\theta\,\tilde{r}_\delta\,\mathrm{d}\theta. \tag{3.6}$$

WJa decomposed the pressure as the summation of the irrotational pressure and a pressure correction, $p = p_\mathrm{i} + p_\mathrm{v}$. Because the irrotational pressure does not contribute to drag, (3.6) can be written in terms of the pressure correction only. The Fourier series for the dimensionless pressure correction can be written as

$$-\tilde{p}_\mathrm{v} = \sum_{k=0}^{\infty} \left(\tilde{C}_k \cos k\theta + \tilde{D}_k \sin k\theta\right). \tag{3.7}$$

Inserting the Fourier series expansion on the azimuthal coordinate θ of the dimensionless pressure correction (3.7) into (3.6), the drag coefficient due to pressure becomes

$$C_{D_p} = \int_0^{2\pi} 2\,\tilde{C}_1 \cos^2\theta\,\tilde{r}_\delta\,\mathrm{d}\theta, \tag{3.8}$$

FIGURE 10. Pressure coefficient c_p as a function of the radial position $\tilde{r}$ from the surface of the rotating cylinder for various pairs of Re and $\tilde{q}$ for a fixed angle θ: 0°, thin solid line; 45°, solid line with △; 90°, dashed line; 135°, dashed line with □; 180°, dashed line with ○; 225°, solid line with ◁; 270°, dashed-dotted line; 315°, dashed line with ×. The pressure coefficient profile given in (3.3) from the exact solution of the equations of motion for a purely rotary flow due to the spinning of the cylinder under the absence of the free stream is also presented (thick solid line). This pressure profile is independent of θ. The average position of the outer edge of the vortical region $\tilde{r}_\delta$ corresponding to the 1% criterion is included (vertical dashed line).

where the orthogonality property of sines and cosines has been applied. Integrating
(3.8) we obtain

$$C_{D_p} = 2\pi \tilde{r}_\delta \tilde{C}_1. \tag{3.9}$$

By equating the power of the pressure correction with the power of the shear stress
discrepancy, WJa found an expression for the coefficient $\tilde{C}_1$. Substitution into (3.9)
yields an expression for the pressure drag coefficient

$$C_{D_p} = \frac{8\pi}{Re}. \tag{3.10}$$

Notice that (3.10) is independent of the tangential velocity $\tilde{q}$.

The outer edge of the vortical region was identified such that the vorticity magnitude
at this position is approximately 1% of the maximum vorticity magnitude. The choice
of this cutoff value was rather arbitrary and it is acknowledged that moderate changes
on this percentage may produce large variations in the thickness and shape of the
vortical region. The introduction in this section of the expression for the pressure
drag coefficient by WJa motivates an alternative way of specifying the thickness of
the vortical region δ/a. This approach is explained in the oncoming paragraphs.

Using the flow field obtained from the numerical simulations, the numerical value of
the pressure drag coefficient C_{D_p} can be computed on a cylindrical surface concentric
with the rotating circular cylinder integrating numerically the pressure field at this
radial position. In other words, we propose to compute the following integral

$$C_{D_p} = -\int_0^{2\pi} 2\,\tilde{p}\cos\theta\,\tilde{r}\,\mathrm{d}\theta, \tag{3.11}$$

for several radial positions $\tilde{r}$, based on the pressure distribution determined in the
numerical solution. The radial position of the outer edge of the vortical region $\tilde{r}_\delta$ is
thus determined by the value of $\tilde{r}$ for which the numerical pressure drag coefficient
C_{D_p} integrated from (3.11) matches the theoretical value obtained in (3.10) for the
pressure drag coefficient at the outer edge of the vortical region as obtained from
the VCVPF theory of WJa. The value predicted in (3.10) actually determines two
interceptions with the numerical profile, one close to the wall and one far from the
wall. In all cases, the interception close to the wall was chosen to set the position of
the outer edge of the vortical region, $\tilde{r}_\delta$. Hence, an effective value of the thickness
of the vortical region δ_D/a is defined (designated as δ_{D_1}/a in WJa). Nevertheless, the
outer interception determines drag due to pressure on that large circle. In the region
close to the second interception, the numerical profile C_{D_p} versus $\tilde{r}$ flattens out (see
figure 11) and the value defined in (3.10) fairly describes the numerical results.
This second interception is discussed in more detail by WJa, who designate the
corresponding thickness of the vortical region as δ_{D_2}/a in their work.

The pressure drag coefficient C_{D_p} computed from the numerical solution using (3.11)
as a function of $\tilde{r}$ is presented in figure 11 for various Re and $\tilde{q}$. Its magnitude tends
to zero slowly as $\tilde{r}$ goes to the outer boundaries. For the pressure drag coefficient,
the graphs reach a maximum close to the wall. Then, the drag coefficient starts
decreasing as $\tilde{r}$ increases. Also, it is remarkable that the pressure drag force changes
its direction when $\tilde{r}$ changes. Close to the wall, the drag force points in the opposite
direction of the free-stream velocity vector. By increasing $\tilde{r}$, the drag force reaches
a magnitude of zero and then changes its direction. In addition, figure 11 shows the
radial position (symbol ●) closest to the wall where the predictions by the model of

FIGURE 11. Pressure drag coefficient C_{D_p} as a function of the radial position $\tilde{r}$ (solid line) as computed from the numerical solution using (3.11) for various Re and $\tilde{q}$. The symbol $\bullet$ indicates the theoretical value of C_{D_p} as predicted from (3.10) proposed by WJa for the radial position of the outer edge of the vortical region where their theory and the numerical results coincide.

WJa for the pressure drag coefficient at the edge of the vortical region (3.10) intercept the numerical profiles.

Table 5 shows the results for the radial position $\tilde{r}_\delta$ and the thickness of the vortical region δ_D/a corresponding to the described interception. As observed previously with the results from the 1% criterion, for a fixed Re, increasing the peripheral speed $\tilde{q}$ yields the decrease of the radial position $\tilde{r}_\delta$ and the corresponding thickness of the vortical region δ_D/a. Moreover, for a fixed $\tilde{q}$, the increase of Re also decreases $\tilde{r}_\delta$ and, hence, δ_D/a. In addition, table 5 includes the results for the pressure drag coefficient from (3.10) by WJa at the edge of the vortical region $\tilde{r}_\delta$, which are the same as the

Re	$\tilde{q}$	$\tilde{r}_\delta$	δ_D/a	$\tilde{\omega}$ magnitude ratio (%)	C_{D_p} by WJa and from numerical simulations
200	4	0.580	0.161	13.05	0.1257
200	5	0.542	0.084	14.61	0.1257
400	4	0.542	0.083	18.15	0.0628
400	5	0.528	0.055	20.82	0.0628
400	6	0.524	0.047	20.66	0.0628
1000	3	0.528	0.055	20.43	0.0251

TABLE 5. Radial position of the outer edge of the vortical region $\tilde{r}_\delta$ and corresponding effective vortical region thickness δ_D/a for which the pressure drag coefficient C_{D_p} at the edge of the vortical region by WJa given in (3.10) matches the numerical profile obtained with (3.11) for various pairs of Re and $\tilde{q}$. These values of $\tilde{r}_\delta$ represent the interception close to the wall. The respective values of C_{D_p} are presented as well. In addition, the percentages of the maximum vorticity magnitude corresponding to the values of $\tilde{r}_\delta$ and δ_D/a according to the procedure described in the previous section to define the edge of the vortical region are included.

values determined through numerical integration of (3.11) for $\tilde{r}_\delta$. Figure 11 indicates the interceptions estimated for every pair of Re and $\tilde{q}$. In the case of the analysis due to Glauert (1957), it predicts a zero pressure drag coefficient, which is the outcome from the classical irrotational flow past a circular cylinder with circulation. Table 5 also presents the percentage of the maximum vorticity magnitude corresponding to the value of δ_D/a for the respective pair of Re and $\tilde{q}$ according to the procedure set in the previous section to define the edge of the vortical region. In other words, if the former criterion were used, the percentages indicated in table 5 would have to be prescribed in order to obtain the same uniform (average) radial position and uniform (average) vortical region thickness. In each case, the percentage is greater than 1% and, therefore, the uniform vortical region thickness δ_D/a is thinner than the corresponding thickness attained with the former 1% criterion (see table 3) since, roughly speaking, the vorticity magnitude declines as the distance from the surface of the cylinder increases. For the second interception, the respective percentages of the maximum vorticity magnitude (not shown in table 5) lie within the interval 0.003% and 1%. The effect of the rotation of the cylinder on the irrotational flow of a viscous fluid outside the vortical region can be rendered through the circulatory velocity at the edge of the vortical region. For potential flow past a circular cylinder of radius a with circulation $\Gamma (= 2aU_0\tilde{\Gamma})$, the circulatory velocity $\tilde{Q}$ at any radial position $r \geqslant a$ is obtained directly from the corresponding expression for the tangential velocity field. It is defined as,

$$\tilde{Q} \equiv \frac{\Gamma}{2\pi r U_0} = \frac{\tilde{\Gamma}}{2\pi\tilde{r}}, \qquad (3.12)$$

in dimensionless form. If the existence of a vortical region attached to the surface of the cylinder comes into play, outside this region, irrotational flow of a viscous fluid can be assumed and (3.12) holds in this external zone. In particular, at the outer edge of the vortical region $\tilde{r}_\delta$, the circulatory velocity is designated as $\tilde{Q}_\delta$. From the numerical solution, the tangential velocity field can be specified for the whole domain. Knowing a set of discrete values for the dimensionless tangential velocity profile on the edge of the vortical region $\tilde{r}_\delta$, the dimensionless circulatory velocity $\tilde{Q}_\delta$ is obtained applying a discrete Fourier transform. The term in the discrete Fourier series independent of θ approximates $\tilde{Q}_\delta$ (i.e. the arithmetic average of the set of

Re	$\tilde{q}$	$\tilde{Q}_\delta$ from numerical simulations	$\tilde{Q}_\delta$ by WJa	$\tilde{Q}_\delta$ by Glauert (1957)
200	4	2.6383	2.6543	3.1994
200	5	4.1270	3.9884	4.3741
400	4	2.9873	2.8930	3.1994
400	5	4.2768	4.1102	4.3741
400	6	5.3669	5.2108	5.4850
1000	3	2.1941	1.7267	1.8800

TABLE 6. Comparison between the circulatory velocity $\tilde{Q}_\delta$ at the edge of the vortical region from the numerical simulation with predictions from (3.14) proposed by WJa and from (3.13) presented by Glauert (1957) for various Re and $\tilde{q}$. The value of $\tilde{Q}_\delta$ from the numerical simulations is obtained as the average of a set of discrete values of the dimensionless tangential velocity field at the outer edge of the vortical region, $\tilde{r}_\delta$. The radial position of the outer edge of the vortical region $\tilde{r}_\delta$ is determined by matching the value of C_{D_p} by WJa in (3.10) with the corresponding numerical profile from (3.11). These values of $\tilde{r}_\delta$ and the respective thicknesses δ_D/a are given in table 5 and correspond to the interception close to the wall.

discrete values for the tangential velocity). The reason is that the tangential velocity profile for potential flow past a circular cylinder with circulation is a constant minus a term proportional to $\sin\theta$ for a fixed radial position. By definition, this constant term represents $\tilde{Q}_\delta$ and, hence, the circulatory velocity may be approximated by the constant term of the Fourier series for the tangential velocity.

Glauert (1957) proposed a series solution that relates the circulatory velocity $\tilde{Q}_\delta$ with the cylinder tangential velocity $\tilde{q}$:

$$\frac{\tilde{Q}_\delta}{\tilde{q}} = 1 - \frac{3}{\tilde{q}^2} - \frac{3.24}{\tilde{q}^4} \dots . \tag{3.13}$$

Through his analysis, Glauert considered a very thin boundary layer, thus neglecting its thickness. Therefore, the circulatory velocity $\tilde{Q}_\delta$ is required at the surface of the rotating cylinder in the context of Glauert's formulation.

WJa presented an expression for $\tilde{Q}_\delta$ as a result of the simple modification of Glauert's boundary-layer analysis to account for the effect of the irrotational rotary component of the flow of a viscous fluid in the interior of the vortical region.

$$\frac{\tilde{Q}_\delta}{\tilde{q}} = \frac{1}{1 + \delta/a} - \frac{3}{\tilde{q}^2} - \frac{3.23}{\tilde{q}^4}\left(1 - 0.803\frac{\delta}{a}\right) \dots . \tag{3.14}$$

This expression takes into account a non-zero vortical region thickness, δ/a. Then, an appropriate value for this parameter is required. The expressions (3.13) and (3.14) by Glauert (1957) and WJa, respectively, represent two different ways of linking the circulatory velocity at the edge of the vortical region and thus the circulation of the irrotational flow of a viscous fluid with the actual peripheral speed at the surface of the rotating cylinder. These expressions stem from the analysis of the boundary layer around the rotating body.

Table 6 shows the numerical results for $\tilde{Q}_\delta$ at the edge of the vortical region and the comparison with the predictions of (3.14) by WJa and also with Glauert's solution (3.13) for various Re and $\tilde{q}$. The numerical results and the predictions from WJa are determined using the vortical region thickness δ_D/a obtained from matching C_{D_p} given in (3.10) with the corresponding numerical profile from (3.11). These values of

δ_D/a were given in table 5 and represent the interception close to the wall. Table 6 indicates that the values predicted using (3.14) due to WJa and the values computed from Glauert's series reasonably approach the results obtained from the numerical simulations for every pair of Re and $\tilde{q}$. Notice that the greatest discrepancy between the predictions of WJa and the numerical results occurs for $Re = 1000$ and $\tilde{q} = 3$, which is the lowest rotational speed considered. WJa point out that for this pair of Re and $\tilde{q}$, their model and the model of Glauert (1957) are not anticipated to approach the true values for C_{L_p} and C_T since the predicted $\tilde{Q}_\delta < 2$ and separation is likely to occur. In the case of Glauert's predictions, the largest relative difference occurs for the lowest Re, i.e. $Re = 200$, and $\tilde{q} = 4$. This may be considered the case where the vorticity effects become more accentuated. For the various pairs of Re and $\tilde{q}$, the observed discrepancies between the theoretical predictions and the numerical results may be influenced by the fact that the vortical regions being considered are quite thick, whereas the theoretical development proposed by Glauert (1957) neglects the boundary-layer thickness. Similarly, the approach by WJa, even though introducing the vortical region thickness δ/a in the expressions for $\tilde{Q}_\delta$ and C_{D_p}, still assumes $\delta/a \ll 1$. It is also noteworthy that for a fixed $\tilde{q}$, the circulatory velocity at the edge of the vortical region $\tilde{Q}_\delta$ increases with the rise of Re. While this trend is followed by the approach of WJa, the predictions of the model proposed by Glauert (1957) are unaffected by the value of Re. For a fixed Re, the numerical results and both theoretical results increase as $\tilde{q}$ increases.

3.5. *Viscous dissipation*

The dissipation represents the work done by the internal viscous stress. The dissipation may be defined by the following expression

$$\mathscr{D} \equiv \int_V 2\mu \boldsymbol{D}\!:\!\boldsymbol{D}\, \mathrm{d}V. \tag{3.15}$$

In dimensionless form, this expression becomes,

$$\tilde{\mathscr{D}} \equiv \int_{\tilde{V}} \frac{2}{Re}\tilde{\boldsymbol{D}}\!:\!\tilde{\boldsymbol{D}}\, \mathrm{d}\tilde{V}, \tag{3.16}$$

where $\tilde{\boldsymbol{D}}$ is the dimensionless rate of strain tensor.

The evaluation of (3.16) is performed numerically using the velocity field determined from the numerical experiments. The domain is split into two zones: inside the vortical region and outside the vortical region. The dissipation values computed in each region add up to the total dissipation.

WJa showed that the dissipation for the irrotational flow of a viscous fluid past a circular cylinder with circulation can be computed as

$$\tilde{\mathscr{D}} = \frac{8\pi}{Re}\left(1 + 2\tilde{r}_\delta^2 \tilde{Q}_\delta^2\right), \tag{3.17}$$

in dimensionless form. The product $\tilde{r}_\delta \tilde{Q}_\delta$ is proportional to the dimensionless circulation (see identity (3.12)), which, for potential flow, is constant over any contour enclosing the rotating circular cylinder. Since WJa proposed expression (3.14) to compute the circulatory velocity at the edge of the vortical region $\tilde{Q}_\delta$, the circulation is determined from (3.12) using this value at the corresponding position $\tilde{r}_\delta$. In this case, the radial position of the outer edge of the vortical region $\tilde{r}_\delta$ is determined by matching C_{D_p} as proposed by WJa in (3.10) with the corresponding numerical results

		$\tilde{\mathscr{D}}$ from numerical simulations			
Re	$\tilde{q}$	Inside VR	Outside VR	Total	$\tilde{\mathscr{D}}$ by WJa
200	4	1.1867	0.5594	1.7461	0.7213
200	5	1.2701	1.3000	2.5701	1.3001
400	4	0.6659	0.3881	1.0541	0.3718
400	5	0.7608	0.7191	1.4798	0.6547
400	6	0.8289	1.0533	1.8822	0.9997
1000	3	0.2322	0.1128	0.3451	0.0669

TABLE 7. Comparison between the numerical results for the dissipation $\tilde{\mathscr{D}}$ determined through numerical integration of (3.16) and the predictions from (3.17) proposed by WJa assuming irrotational flow of a viscous fluid in the entire domain for various *Re* and $\tilde{q}$. Computed contributions from inside and outside the vortical region (VR) are included. The radial position of the outer edge of the vortical region $\tilde{r}_\delta$ is determined by matching C_{D_p} given by the approach of WJa in (3.10) and the corresponding numerical results computed from (3.11). These values of $\tilde{r}_\delta$ and their respective thicknesses δ_D/a represent the interception close to the wall. Their magnitudes are given in table 5.

obtained from (3.11). These values of $\tilde{r}_\delta$ correspond to the interception close to the wall and give rise to the thickness δ_D/a.

Table 7 shows the computed results for the viscous dissipation obtained with (3.16) for the whole computational domain along with the predictions of (3.17). For this case, the dimensionless circulatory velocity $\tilde{Q}_\delta$ on the edge of the vortical region is specified from (3.14) as presented in the work of WJa. The results are presented for various *Re* and $\tilde{q}$. The contributions from inside and outside the vortical region to the dissipation as computed through (3.16) are included as well. The theoretical results included in table 7 are closer to the viscous dissipation computed numerically in the region outside the vortical region than to the total numerical dissipation computed in the whole fluid domain. Moreover, the numerical viscous dissipation computed in the whole fluid domain is significantly greater than the theoretical prediction in all the cases. This trend may be explained by the fact that (3.17) is obtained by WJa considering irrotational flow of a viscous fluid in the whole domain, thus neglecting the thickness of the vortical region. Then, the predicted values are anticipated to be lower than the computed values for the total viscous dissipation, which incorporates the contribution from the vortical region. Furthermore, for a fixed *Re*, the dissipation values computed from the numerical simulations and the predicted ones increase when $\tilde{q}$ increases. The trend is reversed for a fixed $\tilde{q}$ while increasing *Re*, yielding attenuation of the viscous effects.

3.6. *Pressure lift and torque on the rotating cylinder*

One of the most important features regarding the streaming flow past a rotating circular cylinder is the generation of lift on this body. This phenomenon is usually known as the Magnus effect. As mentioned above, the total lift generated on a body can be decomposed into its pressure and friction components. Glauert (1957) calculated the pressure lift coefficient from the classical expression used in aerodynamics:

$$C_{L_p} = \frac{\rho U_0 \Gamma}{\rho U_0^2 a} = 2\tilde{\Gamma}, \qquad (3.18)$$

Re	$\tilde{q}$	$\tilde{r}_\delta$	δ_L/a	C_{L_p} by WJa and from numerical simulations	C_{L_p} by Glauert (1957)
200	4	0.573	0.145	−16.9612	−20.1023
200	5	0.522	0.043	−26.1826	−27.4832
400	4	0.556	0.112	−17.6095	−20.1023
400	5	0.518	0.035	−26.4147	−27.4832
400	6	0.519	0.038	−33.0868	−34.4633
1000	3	0.542	0.084	−10.4085	−11.8124

TABLE 8. Radial position of the outer edge of the vortical region $\tilde{r}_\delta$ and the corresponding thickness of the vortical region δ_L/a determined by matching the numerical result for the pressure lift coefficient C_{L_p} on the cylinder with (3.20) proposed by WJa for various pairs of Re and $\tilde{q}$. The theoretical predictions from the analysis of Glauert (1957) for C_{L_p} on the cylinder according to (3.19) are also presented.

where $\Gamma = 2aU_0\tilde{\Gamma}$. Using identity (3.12), the dimensionless circulation $\tilde{\Gamma}$ can be expressed as a function of $\tilde{Q}_\delta$. Since Glauert's approach neglects the thickness of the vortical region, the circulatory velocity $\tilde{Q}_\delta$ given in (3.13) is determined on the surface of the rotating cylinder. For this position, (3.18) becomes

$$C_{L_p} = 2\pi\tilde{Q}_\delta, \qquad (3.19)$$

where $\tilde{Q}_\delta$ is determined from (3.13) obtained by Glauert.

The simple modification of Glauert's model by WJa yields the following expression for the pressure lift coefficient on the surface of the circular cylinder:

$$C_{L_p} = 2\pi\tilde{q}\left[\frac{1}{1+\delta/a} - \frac{3}{\tilde{q}^2} - \frac{3.23}{\tilde{q}^4}\left(1 - 0.803\frac{\delta}{a}\right)\right]. \qquad (3.20)$$

A new effective vortical region thickness can be determined from (3.20) using the value of C_{L_p} on the rotating cylinder from the numerical results. This approach is also discussed by WJa. This new effective vortical region thickness is designated as δ_L/a. Then, δ_L/a corresponds to the thickness for which the pressure lift on the rotating cylinder predicted by WJa equals the corresponding numerical result (see table 4). Table 8 presents the results for the vortical region thickness δ_L/a and the respective radial positions $\tilde{r}_\delta$. As Re increases, δ_L/a decreases for a fixed $\tilde{q}$; as $\tilde{q}$ increases for a fixed Re, δ_L/a generally decreases. The values of δ_L/a given in table 8 show the same order of magnitude as the values of δ_D/a from table 5 which we determined by matching the theoretical pressure drag coefficient C_{D_p} at the edge of the vortical region from WJa and the corresponding numerical results. Table 8 also includes the predictions from Glauert's model for C_{L_p} on the rotating cylinder. The results indicate that the value of C_{L_p} determined numerically and the predictions increase as the peripheral speed $\tilde{q}$ increases, for a fixed Re. Previous results have shown that the circulatory velocity at the edge of the vortical region $\tilde{Q}_\delta$ increases with $\tilde{q}$ (table 6). Since the circulation $\tilde{\Gamma}$ is proportional to $\tilde{Q}_\delta$, as indicated in (3.12), C_{L_p} increases with $\tilde{q}$. A similar trend is observed when $\tilde{q}$ is fixed and Re increases, except for Glauert's results. Although it is not explicit in (3.14) and (3.20), WJa's approach indeed takes into account the effect of Re in the pressure lift coefficient through the vortical region thickness δ/a. In contrast, not only is Glauert's expression for the circulatory velocity at the edge of the vortical region $\tilde{Q}_\delta$ explicitly independent

Re	$\tilde{q}$	C_T from numerical simulations	C_T by WJa	C_T by Glauert (1957)
200	4	0.4527	0.3895	0.2149
200	5	0.5139	0.4655	0.1945
400	4	0.2750	0.2372	0.1520
400	5	0.2965	0.2724	0.1376
400	6	0.3156	0.2986	0.1264
1000	3	0.1182	0.0632	0.1081

TABLE 9. Comparison between the numerical results for the torque coefficient C_T on the rotating cylinder and the theoretical values obtained with (3.22) proposed by WJa and with (3.21) presented by Glauert (1957) for various Re and $\tilde{q}$.

of Re but also independent of δ/a; then, the pressure lift coefficient in (3.19) does not change with Re.

In their new boundary-layer analysis, WJb calculate the friction drag and lift on the rotating cylinder. These results are not presented in the work of Glauert (1957), although they can be determined from his analysis with no trouble (WJa).

The torque coefficient on the rotating cylinder is determined computing the torque with respect to the centre of the cylinder created on this body by the surrounding fluid through numerical integration of the viscous shear stress at the surface of the cylinder. The torque coefficient was defined in (2.4). The numerical results for the torque coefficient are presented in table 9. Results from the dimensionless form of the expression given by Glauert (1957) for the torque are included as well. This expression can be written as

$$C_T = \frac{2\pi}{\sqrt{Re}}\left(\tilde{q}^{-1/2} - 0.522\tilde{q}^{-5/2}\right). \tag{3.21}$$

In addition, WJa obtained an expression for the torque in their simple modification of Glauert's analysis. In dimensionlees form, this expression becomes,

$$C_T = 4\pi\left(1 + \frac{\delta}{a}\right)\frac{\tilde{Q}_\delta}{Re} + \frac{2\pi}{\sqrt{Re}}\left(\tilde{Q}_\delta^{-1/2} - 2.022\tilde{Q}_\delta^{-5/2} + \dots\right). \tag{3.22}$$

Results from (3.22) are also included in table 9 using the predicted value of the circulatory velocity at the outer edge of the vortical region $\tilde{Q}_\delta$ given by (3.14). WJa indicate that the torque coefficient is not sensitive to the value of δ/a for $\delta/a \ll 1$. Here, the value of the vortical region thickness δ_L/a as determined from the pressure lift coefficient C_{L_p} on the cylinder is used to compute the torque coefficient C_T from (3.22).

Table 9 indicates that both theoretical approaches underpredict the numerical results for the torque coefficient on the cylinder in all the cases. However, the results from the modified approach by WJa are closer to the numerical values than the predictions from Glauert (1957) and, moreover, represent a fairly good approximation, with the exception of $Re = 1000$ and $\tilde{q} = 3$. This case corresponds to the lower peripheral speed considered in this investigation. As mentioned above, since the predicted $\tilde{Q}_\delta < 2$ for $Re = 1000$ and $\tilde{q} = 3$, the models of Glauert (1957) and WJa are not expected to approximate the true results for C_{L_p} and C_T (see table 6) and separation is likely to occur (WJa). Differences between the results from computations and the theoretical predictions may in part stem from the non-negligible vortical region thickness rendered by the numerical solution. The vortical

Re	$\tilde{q}$	δ_D/a	C_{L_p} by WJa	C_T by WJa
200	4	0.161	−16.6636	0.3878
200	5	0.084	−25.0646	0.4658
400	4	0.083	−18.1886	0.2386
400	5	0.055	−25.8452	0.2728
400	6	0.047	−32.7638	0.2989
1000	3	0.055	−10.8624	0.0718

TABLE 10. Results for the pressure lift coefficient C_{L_p} and the torque coefficient C_T on the cylinder computed from (3.20) and (3.22), respectively, using the effective vortical region thickness δ_D/a determined by matching the pressure drag coefficient at the edge of the vortical region from (3.10) with the corresponding numerical profile from (3.11). These results show good agreement with the values of C_{L_p} and C_T shown in tables 8 and 9, respectively, obtained using the effective thickness δ_L/a from table 8.

region thickness is neglected in Glauert's analysis and is only taken into account in the approximation proposed by WJa through the irrotational rotary component of the velocity in the vortical region. Furthermore, for a fixed value of the dimensionless peripheral speed $\tilde{q}$ the torque coefficient determined from the numerical solution and the predictions from the models consistently decrease as Re increases. In this case, the increase in Re indicates that the effects of viscosity are lessened and, as a consequence, the torque produced by the viscous shear stress acting on the surface of the cylinder decreases its magnitude. For a fixed Re, the increase of $\tilde{q}$ produces the increase in the torque coefficient from the numerical results and the predictions from the approach of WJa. Surprisingly, Glauert's predictions follow a non-physical opposite trend. Comparing the expressions for the torque coefficient by Glauert and by WJa, (3.21) and (3.22), respectively, a term proportional to the product $(1+\delta/a)\tilde{Q}_\delta$ emerges in the latter model. Since $\tilde{Q}_\delta$ increases as $\tilde{q}$ rises, this term is responsible for the correct tendency shown by the approach of WJa.

It was mentioned that the values of the effective vortical region thickness δ_D/a (table 5), obtained by matching C_{D_p} in (3.10) with the corresponding numerical profile, and the values of δ_L/a (table 8), the vortical region thickness determined by matching C_{L_p} on the cylinder from (3.20) with the respective numerical result, showed a similar order of magnitude. The latter effective thickness was used to compute the values of the pressure lift coefficient C_{L_p} and the torque coefficient C_T on the surface of the cylinder. Table 10 presents the values of C_{L_p} and C_T on the rotating cylinder computed from (3.20) and (3.22), respectively, with the effective thickness δ_D/a. Comparing these results with the values of C_{L_p} and C_T on the cylinder obtained with δ_L/a shown in tables 8 and 9, respectively, fair agreement among them is observed. Therefore, the pressure drag coefficient C_{D_p} at the edge of the vortical region, the pressure lift coefficient C_{L_p} on the cylinder and the torque coefficient C_T on the cylinder can be computed using a unique effective thickness δ_D/a for every pair of Re and $\tilde{q}$. Then, it may be said that the two main contributions from the work of WJa, to wit, the VCVPF calculation and the simple modification of Glauert's solution, are bridged by the effective thickness δ_D/a.

4. Concluding remarks

We presented results from the numerical simulations of the two-dimensional incompressible Navier–Stokes equations for streaming flow past a rotating circular

cylinder. The numerical solution of the governing equation was accomplished by means of a commercial computational fluid dynamics package. The numerical experiments were performed for various pairs of Reynolds numbers based on the free-stream velocity Re and dimensionless peripheral speed $\tilde{q}$, namely, $Re = 200$ with $\tilde{q} = 4$ and 5; $Re = 400$ with $\tilde{q} = 4$, 5 and 6, and $Re = 1000$ with $\tilde{q} = 3$. Based on the literature review and previous computations, these values were selected to avoid separation of the vortical region attached to the rotating cylinder, three-dimensional effects and transition to turbulence. From the numerical solution, the vorticity field is computed and used to estimate, through an *ad hoc* criterion, the annular region with thickness $\delta_{1\%}/a$ around the cylinder where vorticity is significant.

Two alternative effective thicknesses of the vortical region are proposed based on the agreement between two parameters presented in the approach of WJa and the corresponding results for every pair of Re and $\tilde{q}$. The first effective thickness δ_D/a comes forward by matching the drag coefficient due to pressure C_{D_p} at the outer edge of the vortical region, determined from VCVPF, with the respective profile computed by numerical integration of the pressure field for different radial positions. The second effective thickness of the vortical region δ_L/a is attained by matching the theoretical lift coefficient due to pressure C_{L_p} on the rotating cylinder with the respective numerical results. With either δ_D/a or δ_L/a, the vortical region is again modelled as an annulus concentric with the rotating cylinder.

The effective thickness δ_D/a is used to compute the circulatory velocity at the outer edge of the vortical region and the viscous dissipation inside and outside the vortical region. These results are compared with predictions from WJa using δ_D/a. The effective thickness δ_L/a is applied in the torque coefficient expression for the cylinder presented by WJa and their results are compared with the numerical values. Furthermore, predictions from the classical boundary-layer analysis of Glauert (1957) are also considered for comparison. Glauert's analysis does not depend upon the thickness of the boundary layer. Some of these results are summarized below.

(i) The values of the effective thicknesses δ_D/a and δ_L/a share the same order of magnitude for every pair of Re and $\tilde{q}$. These two effective thicknesses are thinner than the corresponding values of the uniform thickness $\delta_{1\%}/a$ obtained from the former criterion for all the cases. The trends described by δ_D/a and δ_L/a when the parameters Re and $\tilde{q}$ are varied in turn generally follow the tendencies shown by the former uniform thickness $\delta_{1\%}/a$. For a fixed Re, increasing the peripheral speed $\tilde{q}$ decreases the thickness of the vortical region. This trend is also observed when Re increases for a fixed $\tilde{q}$.

(ii) The predictions of the circulatory velocity at the outer edge of the vortical region $\tilde{Q}_\delta$ from WJa using δ_D/a and from Glauert's analysis reasonably approximate the numerical results. When Re is fixed and $\tilde{q}$ increases, $\tilde{Q}_\delta$ increases in both, numerical and theoretical results. For a fixed $\tilde{q}$, the numerical value of $\tilde{Q}_\delta$ increases as Re rises. The approach of WJa follows this trend while Glauert's solution does not change with Re. Each of these approaches for $\tilde{Q}_\delta$ represents two different links between the circulation of the potential flow outside the vortical region and the peripheral speed of the cylinder $\tilde{q}$.

(iii) The viscous dissipation is predicted in the whole fluid domain by WJa assuming irrotational flow of a viscous fluid. These results are fairly close to the numerical results integrated over the subdomain outside the vortical region and substantially lower than the numerical results for the entire fluid domain, which includes the numerical viscous dissipation in the vortical region. The values of the viscous dissipation determined either from the approach of WJa or from the numerical simulations increase as $\tilde{q}$

increases for a fixed Re. The opposite tendency is followed when Re increases as $\tilde{q}$ remains fixed, hence, lessening the viscous effects.

(iv) The numerical results for the pressure lift coefficient C_{L_p}, which, obviously, coincide with the predictions of WJa computed with the effective thickness δ_L/a, and the results from Glauert's solution increase when $\tilde{q}$ rises for a fixed Re. This trend is also followed by the circulation of the irrotational flow which explains the rise in C_{L_p}. The same tendency is observed on the numerical results and, thus, on the predictions of WJa computed with δ_L/a when $\tilde{q}$ is fixed and Re increases, but it is not followed by Glauert's approach which is independent of Re. The dependency of WJa's model upon the vortical region thickness indirectly considers the effect of Re.

(v) The approaches of WJa, using the effective thickness δ_L/a, and Glauert (1957) underpredict the values of the torque coefficient C_T on the cylinder determined numerically. Nevertheless, the results of the former model are fairly close to the numerical values and represent better predictions than the results from the latter one with the exception of $Re = 1000$ and $\tilde{q} = 3$. For a fixed value of $\tilde{q}$, increasing Re decreases the numerical and theoretical values of C_T. Increasing $\tilde{q}$ for a fixed Re yields the increase of the numerical value of C_T and that predicted by WJa. By contrast, Glauert's approach shows an opposite non-physical tendency. The simple modification of Glauert's solution in the work of WJa allows for their model to follow the physical trend by taking into account the irrotational rotary component of the flow inside the boundary layer.

(vi) Finally, the theoretical values of the pressure lift coefficient C_{L_p} and the torque coefficient C_T on the cylinder by WJa's approach, computed with the effective vortical region thickness δ_D/a, are in close agreement with the former results obtained with the effective thickness δ_L/a. Therefore, a unique effective thickness δ_D/a can be used to compute the parameters C_{D_p} at the edge of the vortical region, C_{L_p} on the rotating cylinder and C_T on the rotating cylinder using the expressions proposed by WJa.

We have shown that, with the choice of the thickness δ_D/a as a unique effective thickness, the simple modification of Glauert's boundary-layer analysis and the viscous correction of viscous potential flow (VCVPF) applied to balance the shear stress discrepancy at the outer edge of the vortical region as proposed by WJa, lead to expressions that exhibit better general agreement with the numerical results than Glauert's original solution. This work provides a novel approach for future studies that attempt to focus on the analysis of boundary layers through computational fluid dynamics.

REFERENCES

Badr, H. M., Coutanceau, M., Dennis, S. C. R. & Ménard, C. 1990 Unsteady flow past a rotating circular cylinder at Reynolds numbers 10^3 and 10^4. *J. Fluid Mech.* **220**, 459–484.

Chew, Y. T., Cheng, M. & Luo, S. C. 1995 A numerical study of flow past a rotating circular cylinder using a hybrid vortex scheme. *J. Fluid Mech.* **299**, 35–71.

CHOU, M. H. 2000 Numerical study of vortex shedding from a rotating cylinder immersed in a uniform flow field. *Intl J. Numer. Meth. Fluids* **32**, 545–567.

ECE, M. C., WALKER, J. D. A. & DOLIGALSKI, T. L. 1984 The boundary layer on an impulsively started rotating and translating cylinder. *Phys. Fluids* **27**, 1077–1089.

FLUENT® 6.1. 2003 *User's Guide*. Fluent, Lebanon, NH.

GLAUERT, M. B. 1957 The flow past a rapidly rotating circular cylinder. *Proc. R. Soc. Lond*. A **242**, 108–115.

HE, J.-W., GLOWINSKY, R., METCALFE, R., NORDLANDER, A. & PERIAUX, J. 2000 Active control and drag optimization for flow past a circular cylinder. *J. Comput. Phys.* **163**, 83–117.

INGHAM, D. B. 1983 Steady flow past a rotating cylinder. *Comput. Fluids* **11**, 351–366.

INGHAM, D. B. & TANG, T. 1990 A numerical investigation into the steady flow past a rotating circular cylinder at low and intermediate Reynolds numbers. *J. Comput. Phys.* **87**, 91–107.

JOSEPH, D. D. & WANG, J. 2004 The dissipation approximation and viscous potential flow. *J. Fluid Mech.* **505**, 365–377.

KANG, S., CHOI, H. & LEE, S. 1999 Laminar flow past a rotating circular cylinder. *Phys. Fluids* **11**, 3312–3321.

MITTAL, S. & KUMAR, B. 2003 Flow past a rotating cylinder. *J. Fluid Mech.* **476**, 303–334.

MOORE, D. W. 1957 The flow past a rapidly rotating circular cylinder. *J. Fluid Mech.* **2**, 541–550.

NAIR, M. T., SENGUPTA, T. K. & CHAUHAN, U. S. 1998 Flow past rotating cylinders at high Reynolds numbers using higher order upwind scheme. *Comput. Fluids* **27**, 47–70.

PANTON, R. 1984 *Incompressible Flow*. John Wiley.

TANG, T. & INGHAM, D. B. 1991 On steady flow past a rotating circular cylinder at Reynolds numbers 60 and 100. *Comput. Fluids* **19**, 217–230.

TOKUMARU, P. T. & DIMOTAKIS, P. E. 1993 The lift of a cylinder executing rotary motions in a uniform flow. *J. Fluid Mech.* **255**, 1–10.

WANG, J. & JOSEPH, D. D. 2006a Pressure corrections for the effects of viscosity on the irrotational flow outside Prandtl's boundary layer. *J. Fluid Mech.* **557**, 145–165.

WANG, J. & JOSEPH, D. D. 2006b Boundary-layer analysis for effects of viscosity on the irrotational flow induced by a rapidly rotating cylinder in a uniform stream. *J. Fluid Mech.* **557**, 167–190.

WANG, J., JOSEPH, D. D. & FUNADA, T. 2005 Pressure corrections for potential flow analysis of capillary instability of viscous fluids. *J. Fluid Mech.* **522**, 383–394.